Journal of Fluids and Structures (1999) **13,** 1041–1067
Article No.: jfls.1999.0248, available online at http://www.idealibrary.com on IDEAL®

TURBULENT ELLIPTIC WAKES

M. Kiya and Y. Abe

Graduate School of Engineering, Hokkaido University
Sapporo 060-8628, Japan

(Received 19 October 1998 and in revised form 14 June 1999)

This paper describes results of an experimental study on turbulent wake of an elliptic disk set normal to the main flow, whose major diameter is 2·0 or 3·0 minor diameters, Reynolds number being $2{\cdot}0 \times 10^4$ on the basis of the minor diameter D. Two periodic components of velocity fluctuations were found in the wake. One is centred around the minor plane, being due to the alternate shedding of rolled-up, hairpin-like vortices. The other is centred around the major plane, which is likely to be due to a meandering motion of the wake. The axis switching, which is a cross-over of half-widths in the major and minor planes plotted against the streamwise distance, occurred at approximately 4·0D downstream of the disk. The mechanism of the axis switching is different from that in elliptic jets, and it is proposed that it is due to a difference in the growth rate of the fundamental Fourier modes in the minor and major planes. The structure of the wake is studied by flow visualization and a survey of the time-mean velocity, turbulence intensities and Reynolds shear stresses. Wavelet analysis of the velocity fluctuations disclosed a low-frequency unsteadiness in the wake. This unsteadiness has different representative frequencies in the major and minor planes, being approximately one-fifth of the frequency of the corresponding periodic component in both planes. © 1999 Academic Press

1. INTRODUCTION

Wakes of three-dimensional bluff bodies have been studied mostly for axisymmetric one such as spheres and circular disks. In the wakes of these axisymmetric bodies, there are three modes of instability (Berger *et al.* 1990). The first is the shear layer instability, which is the Kelvin-Helmholtz instability of the shear layer near the separation edge. The second is the pumping mode which is manifested as an axisymmetric oscillation of the recirculation zone behind the body. The third, which is the major mode of instability, is a helical mode, generating a helical vortex structure in the wake. Monkewitz (1988) argues that the frequency of periodic velocity fluctuations in the wake of a sphere is associated with the helical mode of instability in the axisymmetric steady near wake. His analysis yields the frequency of the most unstable mode which is consistent with the experimentally observed vortex-shedding frequency.

The helical structures in the wake of a sphere are experimentally demonstrated by Taneda (1978) and Cannon *et al.* (1993). Hairpin-like vortices are also found in the wake of a sphere (Achenbach 1974; Sakamoto & Haniu 1990; Shirayama 1992). The shear layer instability is manifested as the higher branch of bifurcation of Strouhal number plotted against Reynolds number (Kim & Durbin 1988; Sakamoto and Haniu 1990). The lower branch corresponds to the frequencies of the helical or axisymmetric mode.

Statistical properties of the time-mean and fluctuating velocities and pressures in the wake of axisymmetric bodies are obtained by a number of investigators (Hwang & Baldwin 1966; Chavrey 1968; Uberoi & Freymuth 1970; Fuchs *et al.* 1979; Wu and Faeth 1993).

0889–9746/99/101041 + 27 $30.00 © 1999 Academic Press

There are a number of asymmetric bodies in engineering applications. A typical example is the side-view mirrors of cars. The wake of the mirrors passes along the side windows of the cars, producing pressure fluctuations on the windows which may cause noise in the cabin. Thus, it is crucial to clarify the structure of vortices in the wake and the frequency of vortex shedding, if any. Trains and cars are other examples. In cold regions, vortices in the wake of cars fling up snow particles; the snow attached onto the rear side of the cars prevents visibility of winkers and brake indicators. The capony of asymmetric parachutes (Peterson *et al.* 1996) can also be mentioned. However, the structure of turbulent wakes of asymmetric bodies is not clarified yet, at least to the same extent as that of the axisymmetric wakes.

The purpose of the present paper is to study the turbulent wake of an elliptic disk which is set normal to the approaching flow. The elliptic disk is chosen as a simple shape of asymmetric bluff bodies. This has two length scales and smooth variation of curvature along the edge. The latter is not the case for a rectangular plate, which is another simple shape of an asymmetric body.

Apart from engineering applications, the turbulent wake of the elliptic disk deserves study in its own right, because the wake may have novel properties which could not be expected from those of axisymmetric wakes. A few issues of interest are as follows. Is there any periodic vortex shedding from the disk? If any, what is the typical frequency or frequencies? Is there any axis-switching in the wake as in an elliptic jet? If any, is the mechanism the same as that for the elliptic jet? These issues will be resolved in this paper. Moreover, a survey of the time-mean velocities, turbulence intensities and Reynolds shear stresses are made to clarify the turbulence structure in the wake.

2. EXPERIMENTAL APPARATUS AND METHODS

The flow configuration and definition of main symbols are shown in Figure 1. The x-axis is taken in the longitudinal direction, the y-axis along the major axis, and the z-axis along the minor axis. The origin is at the centre of the front face of the disk. The time-mean and

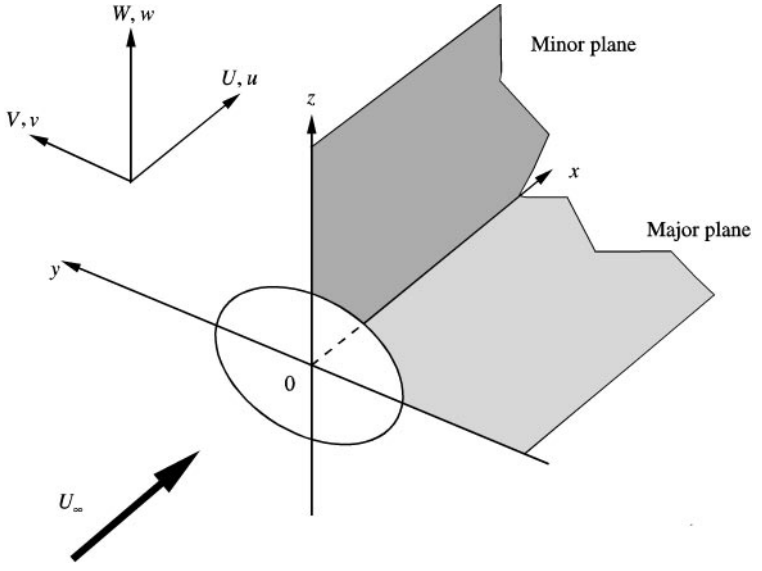

Figure 1. Elliptic disk, coordinate system, major and minor planes and velocity components.

fluctuating velocity components in the x, y and z directions are denoted by U, V, W and u, v, w, respectively. The r.m.s. value of u, v and w will be denoted by u', v' and w'. The (x, y) plane will be referred to as the major plane, while the (x, z) plane as the minor plane. Moreover, variables of flow in the major and minor planes will be denoted by the suffix M and m, respectively.

Experiments were performed in a through-flow wind tunnel with a 30·0 cm wide, 30·0 cm high and 100·0 cm long working section. The flow is introduced into the working section through a bell entrance of 1 : 9 contraction. A filter of glass wool is attached to the inlet of the calming (settling) chamber in which two stages of gauze screens are installed. The free-stream turbulence level is 0·5% at a main-flow velocity U_∞ of 15·0 m/s, which is employed in the present study. The velocity U is uniform within $\pm$ 0·5% of U_∞ in the cross-section at 0·30 m downstream of the inlet of the working section, except for the boundary layers on the tunnel walls. The thickness of the boundary layer at this section, which is turbulent, is approximately 3 cm.

Two elliptic disks of the minor diameter D of 20·0 mm were manufactured by machining from a brass plate of 3·0 mm in thickness. One has the major diameter L of 40·0 mm and the other has $L = 60{\cdot}0$ mm. The disks will be referred to by the aspect ratio AR ($= L/D$), which is 2·0 for the former and 3·0 for the latter. The edge of the disks are bevelled towards the downstream side by the angle of 45·0°.

The elliptic disk was fixed at 0·30 m downstream of the inlet in the middle of the working section by three steel wires of 0·2 mm diameter, as shown in Figure 2. The wires are thin enough for their effects on the wake to be neglected. Moreover, the blockage ratio of the disks is 0·70–1·0%, so that their effects on the wake can also be neglected. No sensible oscillation of the disks was observed during the experiment at the main-flow velocity $U_\infty = 15{\cdot}0$ m/s.

Measurements of the velocity components were made by constant-temperature hot-wire anemometers using an I-wire probe, an X-wire probe, and a split-film probe (TSI Model

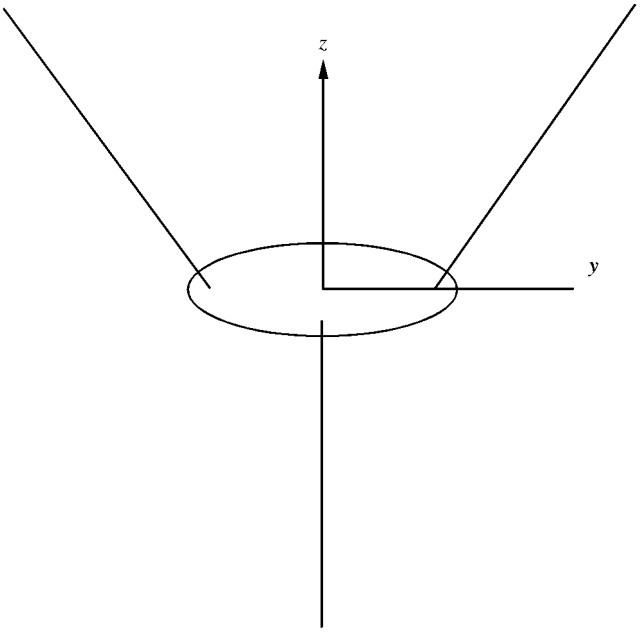

Figure 2. Support of elliptic disk by three thin wires.

1287) which can detect an instantaneous flow reversal. The I- and X-wire probes were tungsten wires of 5 μm diameter with a working length of 1·0 mm. The X-wires were inclined by $\pm 45^\circ$ with respect to the longitudinal direction. Measurements by these hot-wire probes were made only in a region where intermittent reverse flow is negligible. In the region of intermittent reverse flow, the velocity components U and u were detected by the split-film probe (of 132 μm diameter) with the plane of split normal to the longitudinal direction. The instantaneous velocity components were digitized with a time interval of 0·5 ms over 5 s to obtain the time-mean and fluctuating components, while the digitization was made at a shorter interval of 0·1 ms over the time of 1·024 s to obtain the power and cross-spectra. The spectra were calculated by a FFT analyzer. Most of the velocity measurements were made in the major and minor planes.

Hot-wire measurements are likely to be reliable only if the ratio u'/U, say, is less than approximately 0·3, while, if the relative intensity exceeds 0·5, hot-wire results are likely to be highly unreliable (Chandrsuda & Bradshaw 1981). In this study, no corrections were made for the effects of high turbulence intensities on the time-mean and fluctuating velocities, thus results within the band $0{\cdot}3 < u'/U < 0{\cdot}5$ should be taken with reserve. Measurements of U and u' in the major and minor planes at $x/D = 2{\cdot}0$ and 8·0 by the two types of hot-wire probes and the split-film probe revealed that the mean deviation among measured values was within $\pm 0{\cdot}05U_\infty$ and $\pm 0{\cdot}02U_\infty$, respectively, in a region where the reverse-flow time fraction I_r was less than 0·2 (Figure 3). Moreover, the repeatability of the normal velocity components V and W measured by the X-probe was within $\pm 0{\cdot}03U_\infty$, while that of the fluctuating components v' and w' was $\pm 0{\cdot}004U_\infty$. The repeatability of the measured Reynolds shear stresses $-\overline{uv}$ and $-\overline{uw}$ was $\pm 0{\cdot}002U_\infty^2$.

The experiments were made at Reynolds number Re ($=U_\infty D/\nu$, ν is the kinematic viscosity) of $2{\cdot}0 \times 10^4$. Flow visualization was also made in a water channel at a lower Reynolds number Re = 200 to help the interpretation of results of the wind-tunnel experiment. Fluorescent dye was introduced upstream of the disk through a hypodermic needle to impinge onto the stagnation point on the front face. The dye travelled along the front face and eventually entered into the wake from the edge of the disk.

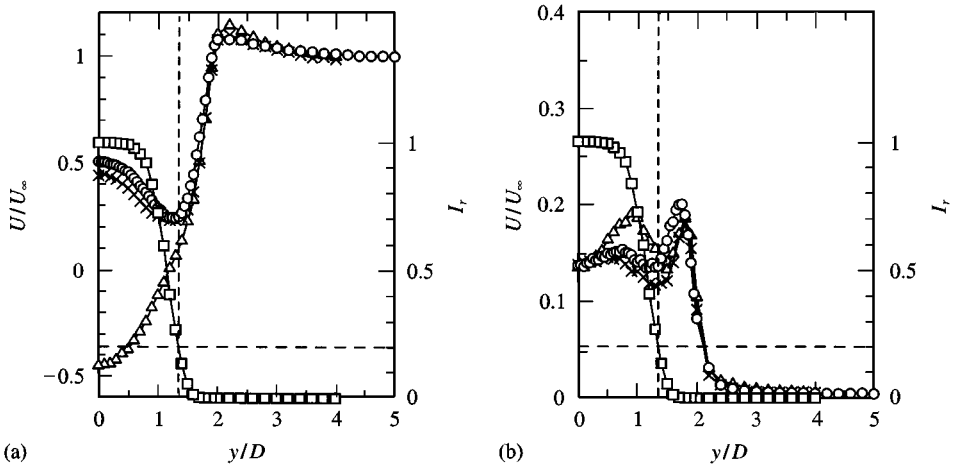

Figure 3. Distributions of (a) time-mean velocity U and (b) fluctuating component u' measured by different probes in the major plane at $x/D = 2{\cdot}0$.△, split-film probe; ○, I-wire probe; ×, X-wire probe; □, reverse-flow time fraction I_r measured by split-film probe.

3. RESULTS

3.1. Flow Visualization

Results of the flow visualization are shown in Figure 4 for the disk of AR = 3·0. The flow pattern in the minor plane in Figure 4(b) shows the alternate shedding of large-scale vortices. These vortices are the hairpin-like vortices in the major plane [Figure 4(a)]. Although the hairpin-like vortices seem to be symmetric, the flow pattern in the major plane is not symmetric but seems to indicate a meandering motion. The above features of the flow pattern are basically the same for the disk of AR = 2·0.

One might expect that an elliptic vortex ring is shed from the edge, generating the hairpin-like vortices by the self-induced deformation and interaction between neighbouring vortex rings as in the case of the elliptic jets (Ho & Gutmark 1987; Hussain & Husain 1989). If this interpretation is correct, the deformed vortex ring should have two planes of symmetry, as shown in figure 26 in Hussain & Husain (1989). The hairpin-like vortices in the wake have no such symmetry. This strongly suggests that the formation of the hairpin-like vortices and their alternate shedding have nothing to do with the self-induced deformation of the elliptic vortex rings but are associated with instability of flow in the near wake.

3.2. Vortex Shedding

The shedding of the hairpin-like vortices in Figure 4 is periodic. This is demonstrated by those power spectra of longitudinal velocity fluctuations $E_u(f)$, f being the frequency, which are shown in Figure 5. The spectrum of u in the outer part of the wake in the minor plane has a sharp peak at a frequency of 80 Hz for the disk of AR = 3·0 [Figure 5(b)]; this frequency will be denoted by F_m. It is surprising that the spectrum of u in the major plane also has a sharp peak at a lower frequency of 45 Hz; this frequency will be denoted by F_M. In

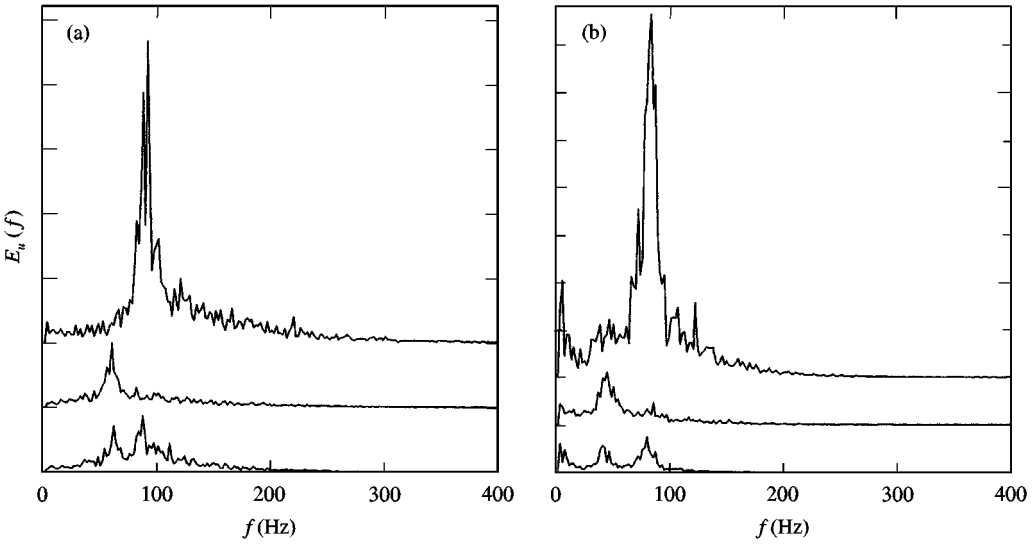

Figure 5. Power spectra of longitudinal velocity fluctuation $E_u(f)$ at $x/D = 4·0$ for (a) AR = 2·0: top curve at $(y/D, z/D) = (0·0, 2·0)$ in minor plane; middle curve at $(y/D, z/D) = (2·0, 0·0)$ in major plane; bottom curve at $(y/D, z/D) = (1·5, 1·5)$, and (b) AR = 3·0: top curve at $(y/D, z/D) = (0·0, 2·5)$ in minor plane; middle curve at $(y/D, z/D) = (2·5, 0·0)$ in major plane; bottom curve at $(y/D, z/D) = (2·0, 2·0)$. Vertical scale is arbitrary linear.

the middle of the major and minor planes, the spectrum has two peaks at the frequencies F_m and F_M. Both spectrum peaks were detected as far as $x/D = 20$. The spectrum peaks are also found for the disk of AR = 2·0, as shown in Figure 5(a). In this case, the peak frequencies are $F_m = 90$ Hz and $F_M = 60$ Hz. The peak frequencies are plotted in Figure 6 against AR in the form of Strouhal number $\mathrm{St}_i = F_i D/U_\infty$, where the suffix i implies M or m. One might expect that St_m is the same for both disks. However, this is not the case, as shown by the solid lines in Figure 6. The solid lines are drawn taking the extended branch of St_i into account. The data were extended to AR < 1·0 in the following way. Assume that D is fixed while L is changed from a value greater than D (AR > 1) to another value less than D (AR < 1). The frequencies F_M and F_m should be interpreted as the peak frequencies

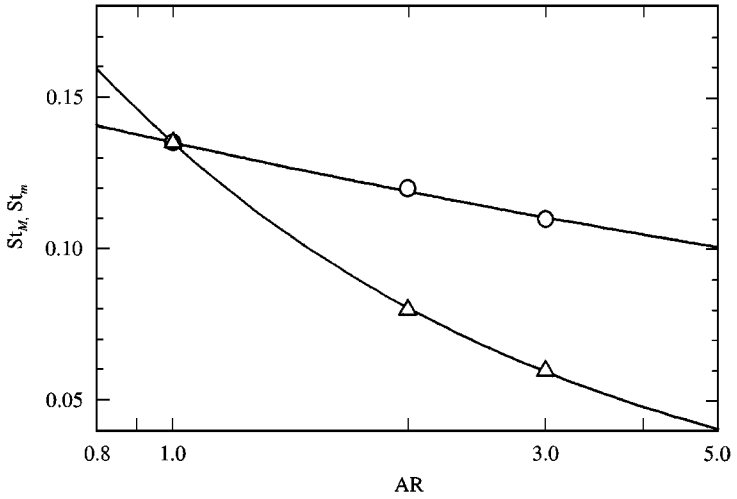

Figure 6. Strouhal numbers of elliptic disks as function of aspect ratio AR. o, St_m; △, St_M. Solid lines are drawn taking into account the extended branch in AR < 1. See text for procedure of the extension.

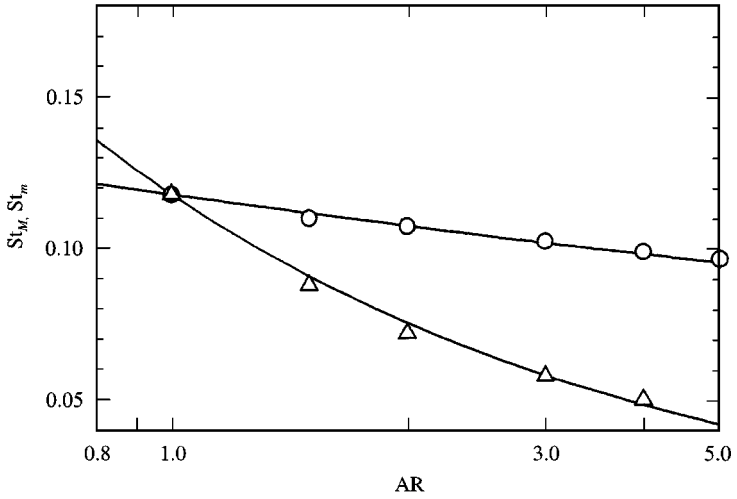

Figure 7. Strouhal numbers of rectangular plates as function of aspect ratio AR. o, St_m; △, St_M. For meaning of solid lines, see caption of Figure 6.

measured in the (x, y) and (x, z) planes, respectively (Figure 1). Thus, for a value of $\mathrm{AR} = \alpha < 1$, St_M is equal to St_m for $\mathrm{AR} = 1/\alpha$ times α, while St_m is equal to St_M for $\mathrm{AR} = 1/\alpha$ times α.

One might also expect that F_M normalized in the form $F_M L/U_\infty$ is the same for both disks, being equal to St_m. However, this again is not the case, as can easily be confirmed from the data in Figure 5. Thus, a universal Strouhal number cannot be constructed by merely adjusting the geometrical length scales.

For the purpose of reference, measurements of the power spectrum were made for thin rectangular plates normal to the main flow in the same wind tunnel. The spectra in the minor and major planes were found to have a sharp peak at different frequencies. These frequencies in the form of St_m and St_M are shown in Figure 7 as a function of AR, in which D and L are the length of the shorter and longer sides, respectively. The Strouhal numbers have the same trend of change and approximately the same value as those for the elliptic disks. This suggests that the mechanism of generation of the periodic components is the same for both the elliptic and rectangular disks. In passing it is worth noting that St_m was found to tend to the value of the two-dimensional normal plate approximately at $\mathrm{AR} = 40{\cdot}0$.

The vortices shed alternately in the minor plane [Figure 4(b)] were confirmed to generate the periodic component F_m. On the other hand, the flow visualization in the major plane [Figure 4(a)] shows no definite vortical structures responsible for the component F_M. This might be due to the difference in Reynolds numbers in the flow visualization ($\mathrm{Re} = 200$) and the wind-tunnel experiment ($\mathrm{Re} = 20000$), that is, this structure might become evident at sufficiently high Reynolds numbers. It is also possible that the component F_M is due to a meandering motion of the wake in the major plane. For convenience of description, however, the structure responsible for F_M will hereinafter be referred to as vortices. This structure will be discussed later in Section 4.

Strouhal numbers St_M and St_m have distributions in (y, z) cross-sections such as shown in Figure 8. In the vicinity of the disk $x/D = 2{\cdot}0$, St_m is observed in a region centred around the minor plane, while St_M appears in a region centred around the major plane. More downstream, the region of St_M shrinks, while the region of St_m enlarges. Thus the hairpin-like vortices in the minor plane appear to be the dominant structure in the near wake. The same features are also observed in the wake of the rectangular plates, as shown in Figure 9.

3.3. Phase Relation, Wavelength and Integral Length Scale

The coherence $\mathrm{coh}^2(f)$ and phase $\Phi(f)$ of u at positions of maximum u' are presented in Figure 10 to obtain the phase relation of the periodic components on both sides of the wake. The phase is 180° in the major plane and -180° in the minor plane at the frequency F_m and F_M, respectively, where the coherence attains a maximum. Thus, the structures which are responsible for the periodic components are shed alternately on either side of the wake in each plane. This is consistent with the shedding of the hairpin-like vortices in minor plane [Figure 4(b)].

The phase velocity of u was obtained in terms of the cross-correlation of u at two points separated by a distance $\Delta x = 0{\cdot}37D$ in the streamwise direction. The time lag τ at which the correlation attains a maximum yields the phase velocity $U_c = \Delta x/\tau$ at the position $x + \Delta x/2$, where x is the position of the upstream probe. The phase velocity can be interpreted as the velocity of convection of rolling-up vortices. The result is shown in Figure 11. The phase velocity in the minor plane U_{cm} decreases with increasing x to a value of approximately $0{\cdot}75U_\infty$ at $x/D \approx 5$. On the other hand, the phase velocity in the major plane U_{cM} approaches to this value from below at the same x/D. This suggests that the end

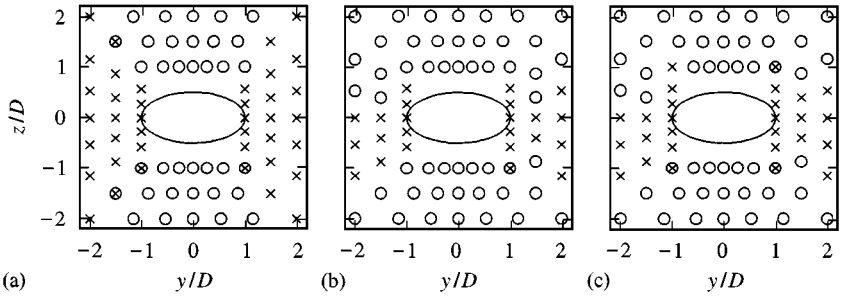

Figure 8. Distribution of St_M and St_m in cross-sections normal to main-flow direction for elliptic disk of AR = 2·0. ×, St_M; o, St_m. In (a), $x/D = 2{\cdot}0$; (b), $x/D = 4{\cdot}0$; (c), $x/D = 6{\cdot}0$.

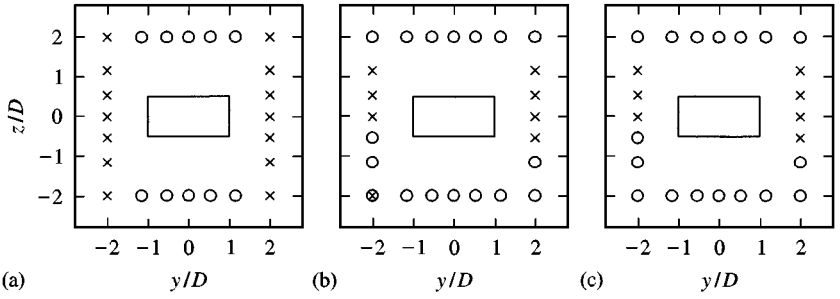

Figure 9. Distribution of St_M and St_m in cross-sections normal to main-flow direction for rectangular plate of AR = 2·0. ×, St_M; o, St_m. In (a), $x/D = 2{\cdot}0$; (b), $x/D = 4{\cdot}0$; (c), $x/D = 6{\cdot}0$.

of the vortex formation region is at $x/D \approx 5{\cdot}0$, downstream of which the phase velocities should slowly increase with increasing x by the decay of the shed vortices.

The wavelength of the velocity fluctuation λ, which can be interpreted as the distance between two consecutive vortices, is obtained as the phase velocity U_c divided by the peak frequency F. The wavelength in the region $x/D = 5 \sim 6$ is approximately $\lambda_m = 6{\cdot}3D$ in the minor plane and $\lambda_M = 9{\cdot}4D$ ($=4{\cdot}7L$) in the major plane for AR = 2·0, while it is $\lambda_m = 6{\cdot}8D$ and $\lambda_M = 12{\cdot}5D$ ($=4{\cdot}2L$) for AR = 3·0. This suggests that the wavelengths λ_M and λ_m approximately scale to the major and minor diameters. The wavelength λ_m is approximately the same as the distance between consecutive hairpin-like vortices in the flow visualization [Figure 4(a)]. On the other hand, the longitudinal length scale of the vortices was 0·6–0·9D in the region $x/D = 5 \sim 6$. This was the same in the minor and major planes for AR = 2·0 and 3·0. It may be noted that the length scale was defined as the integral time scale (which was obtained from the autocorrelation coefficient of u at positions of maximum u') multiplied by the phase velocity.

3.4 Flow Fields

3.4.1. *Overview and time-mean velocities*

Distributions of the time-mean velocity U, turbulence intensity u' and reverse-flow time fraction I_r in the major and minor planes (Figure 12) yield an overview of the flow field for AR = 3·0. These were measured by the split-film probe. I_r is zero at $x/D = 4{\cdot}2$; a plot of I_r on

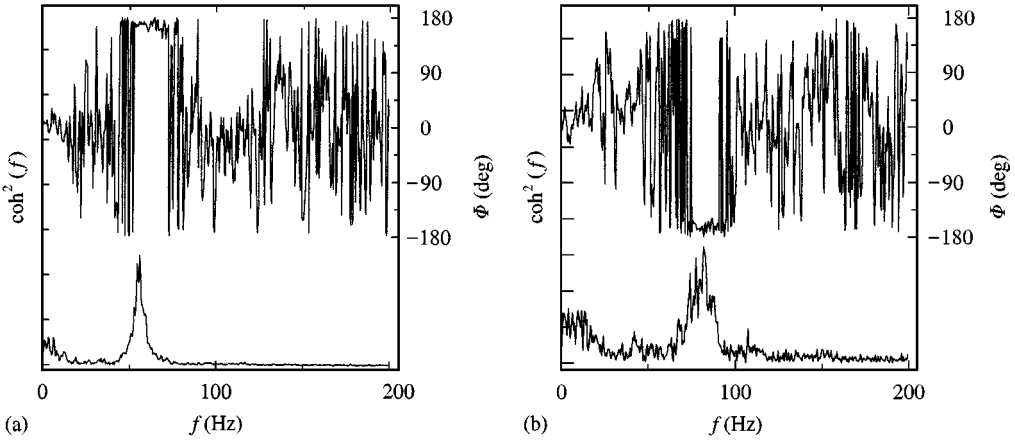

Figure 10. Coherence coh$^2(f)$ and phase $\Phi(f)$ of longitudinal velocity fluctuations at positions of maximum u' at $x/D = 2{\cdot}0$ in (a) major plane and (b) minor plane for AR $= 2{\cdot}0$. Vertical scale for coherence is arbitrary and linear.

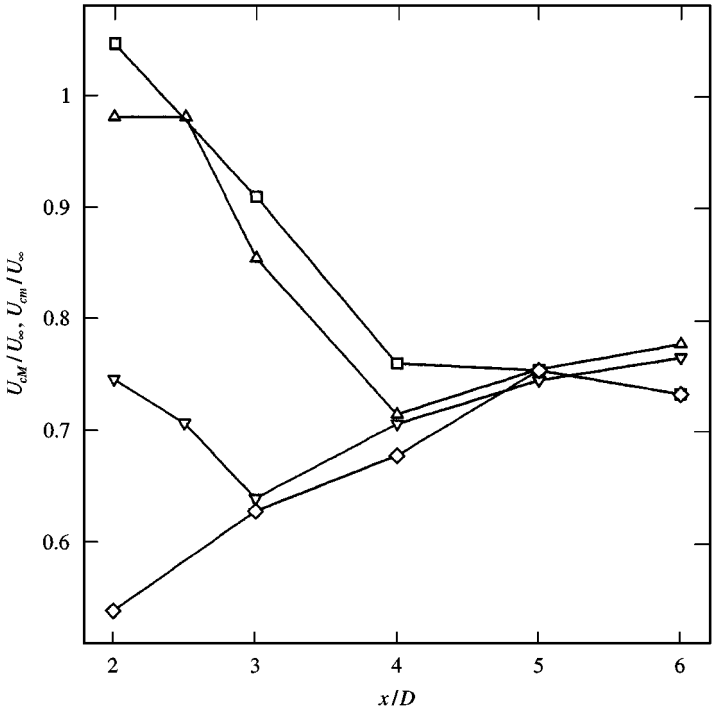

Figure 11. Phase velocity of longitudinal velocity fluctuations at positions of maximum u'. △, U_{cM} (AR $= 2{\cdot}0$); ▽, U_{cM}(AR $= 2{\cdot}0$); □, U_{cM}(AR $= 3{\cdot}0$); ◇, U_{cm} (AR $= 3{\cdot}0$). Solid lines for visual aid only.

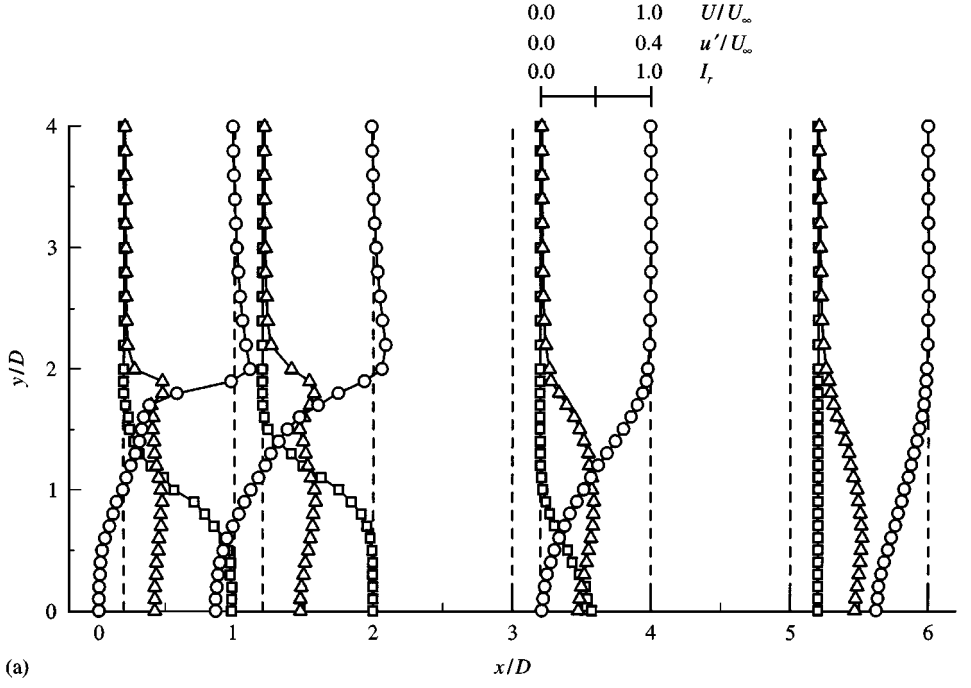

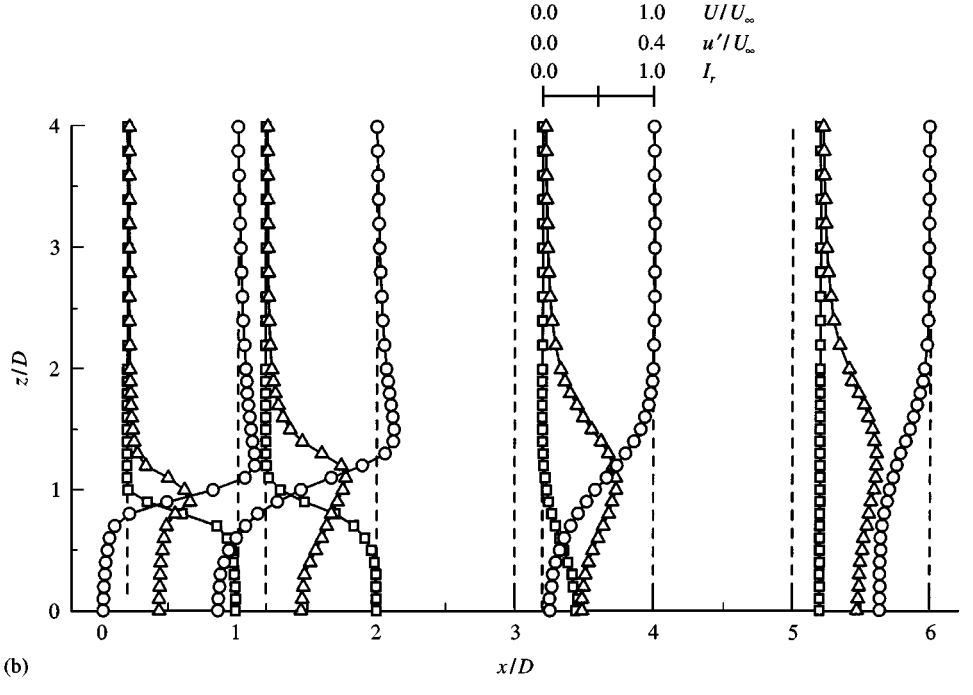

Figure 12. Distributions of U, u' and I_r measured by split-film probe in (a) major plane and (b) minor plane for AR = 3·0: o, U; △, u'; □, I_r.

the wake axis against x (not shown) showed that the end of the recirculating region is approximately at $x/D = 5{\cdot}0$. This was the same for AR $= 2{\cdot}0$. The edge of the wake remains approximately at the same position in the major plane ($y/D = 2{\cdot}0$), while it moves quickly outwards in the minor plane. Moreover, the level of turbulence intensity u' is higher in the minor plane than in the major plane. A maximum of u' appears in a region where I_r is zero, so that its value can reliably measured by the I-wire and the X-wire probes.

Detailed distributions of the time-mean velocities in both planes are shown in Figure 13, where values of V and W only in regions of $I_r < 0{\cdot}2$ are included for the reason mentioned in Section 2. Note that the distributions of U are symmetric and those of V and W are antisymmetric on both sides of the centre of the wake. In the near wake $x/D < 4{\cdot}0$, U, V and W have much complicated distributions due to rapid change in flow direction in the recirculating region.

It is noteworthy that the velocity component W in the minor plane is positive in the region $x/D > 6{\cdot}0$ for $z > 0$ (Figure 13). This does not mean that, in the minor plane, the fluid is entrained out of the wake into the main flow. The positive W can be interpreted in terms of the equation of continuity in the minor plane, i.e. $\partial U/\partial x + (\partial V/\partial y)_{y=0} + \partial W/\partial z = 0$. The term $(\partial V/\partial y)_{y=0}$ is likely to be almost negative in the region $x/D > 6$ as seen in Figure 13, being a function of x and z. Integrating the equation of continuity with respect to z from 0 to an arbitrary positive z, one obtains

$$W(x, z) = -\frac{\partial}{\partial x}\int_0^z U(x, \zeta)\,\mathrm{d}\zeta - \int_0^z \left(\frac{\partial V}{\partial y}\right)_{y=0} \mathrm{d}\zeta, \tag{1}$$

since $W(x, 0) = 0$. The integral in the first term is an increasing function of x in the region $x/D > 6$, so that the first term is negative. On the other hand, the second term is positive in the same region, which overcomes the first term to make $W(x, z)$ positive. Thus, the positive W is brought about by the "squeezing" in the y-direction.

The velocity component V in the major plane is negative in the same region of $x/D > 6{\cdot}0$ for $y > 0$ (Figure 13); this is the case in the far wake of axisymmetric bodies like a sphere or a circular disk. The equation of continuity in the major plane yields $V(x, y)$ of a form similar to equation (1), but the corresponding two terms are likely to be all negative. Thus, the negative V is partly caused by the entrainment of the main-flow fluid into the wake and partly by the "negative" squeezing in the z-direction.

As would be expected, the width of the wake is greater in the major plane than in the minor plane in the near wake $x/D < 4{\cdot}0$. This situation is reversed in a more downstream region $x/D > 5{\cdot}0$. In order to clarify this point, the half-widths b_M and b_m are defined in the major and minor planes as the distance between positions where the velocity defect is equal to a half of that at the centre. The half-widths are plotted against x in Figure 14. The cross-over of b_M and b_m occurs approximately at $x/D = 3{\cdot}8$ for AR $= 2{\cdot}0$ and $x/D = 4{\cdot}2$ for AR $= 3{\cdot}0$. This feature will be referred to as the axis switching. The axis switching is visualized as the rapid outward motion of the hairpin-like vortices in the minor plane and at the same time as the shrinkage of these vortices in the y-direction by longitudinal stretching, as shown in Figure 4.

A similar axis switching has been observed in elliptic jets (Ho & Gutmark 1987; Hussain & Husain 1989). This is interpreted by the self-induced deformation of single elliptic vortex rings of the same aspect ratio. However, this mechanism is not the case in the elliptic wakes. This is because the axis switching in elliptic jets has two planes of symmetry [Figure 26 of Hussain & Husain 1989] while the vortices in the minor plane of the elliptic wakes have no such symmetry. The axis switching in the elliptic wakes, as will be discussed later in Section 4, might be interpreted as the higher growth rate of the most amplified mode in the minor plane than in the major plane.

The velocity defect ΔU in the wake is plotted in Figure 15 against the transverse coordinates normalized in the form y/b_M and z/b_m; the velocity defect is normalized by the velocity defect on the x-axis ΔU_0. The velocity defect has approximately similar distributions in the region $x/D = 12$–20, except for the edges of the wake where experimental uncertainties in ΔU are relatively high. The maximum velocity defect appears in the minor plane.

3.4.2. *Turbulence intensities and Reynolds shear stresses*

Figure 16 shows distributions of the turbulence intensities u', v' and w', and Reynolds shearing stresses $-\overline{uv}$ and $-\overline{uw}$. Note that $-\overline{uv}$ is zero in the minor plane while $-\overline{uv}$ is zero in the major plane by symmetry. Also note that $-\overline{uv}$ and $-\overline{uw}$ are antisymmetric on both sides of the wake axis. The data are presented in a region where I_r is less than 0·2 except for those obtained by the split-film probe.

The level of u' is much higher in the minor plane than in the major plane in the region $x/D < 5{\cdot}0$. This is due to the shedding of the hairpin-like vortices in the minor plane (Figure 4). This is also the reason why the level of $-\overline{uw}$ in the minor plane is higher than that $-\overline{uv}$ in the major plane. The double peak of u' in the major plane at $x/D = 1{\cdot}0$ and 2·0 is associated with two inflection points in the distributions of U at these x positions. The maximum of u', which appears at the position of maximum $|\mathrm{d}U/\mathrm{d}y|$ in the major plane and maximum $|\mathrm{d}U/\mathrm{d}z|$ in the minor plane, is higher than v' and w' because the turbulence is first

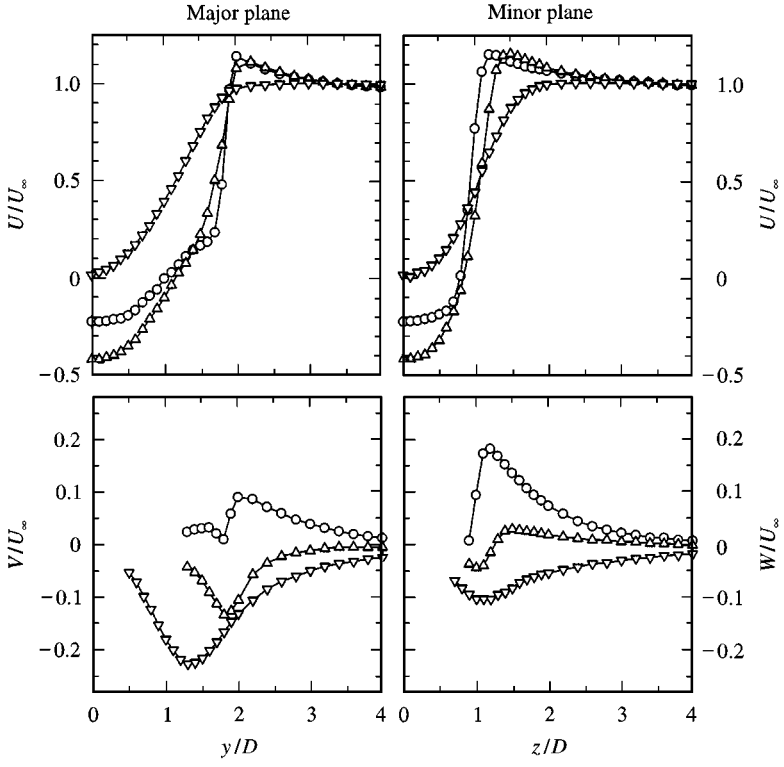

Figure 13. Distributions of U, V and W for AR = 3·0: o, $x/D = 1{\cdot}0$; △, $x/D = 2{\cdot}0$; ▽, $x/D = 4{\cdot}0$. U was measured by split-film probe while V and W were measured by X-wire probe. V and W are shown only in regions where I_r is less than 0·2. Solid lines for visual aid only.

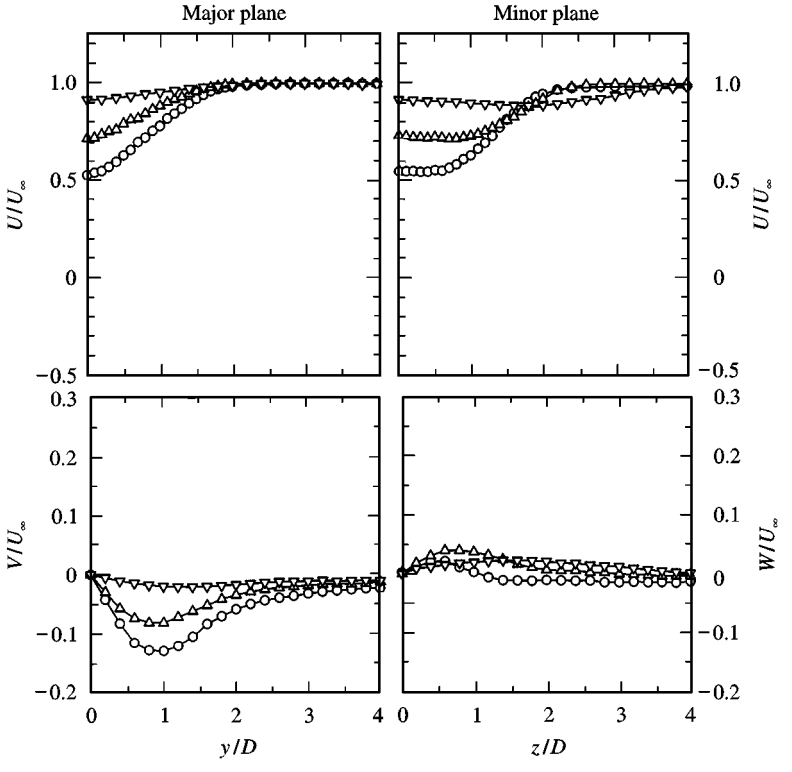

Figure 13. (Continued) Distributions of U, V and W for AR = 3·0. o, x/D = 6·0: △, x/D = 8·0; ▽, x/D = 20·0. U was measured by I-wire probe while V and W were measured by X-wire probe.

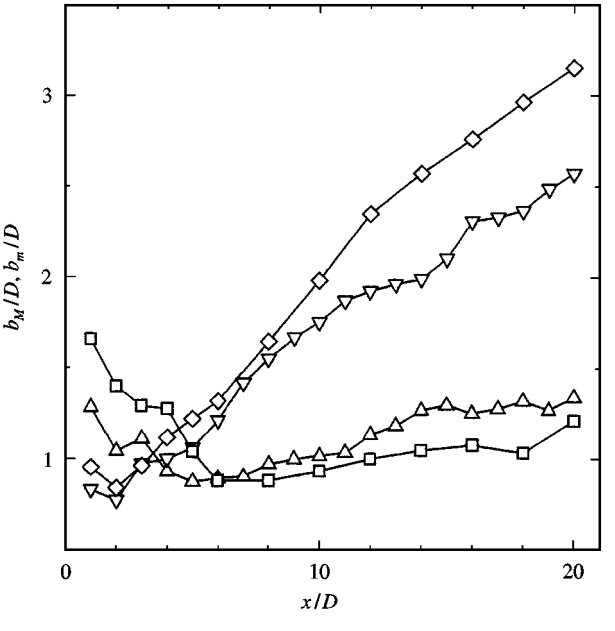

Figure 14. Half-width as function of longitudinal distance: △, b_M (AR = 2·0); ▽, b_m (AR = 2·0); □, b_M (AR = 3·0); ◇, b_m (AR = 3·0). Solid lines for visual aid only.

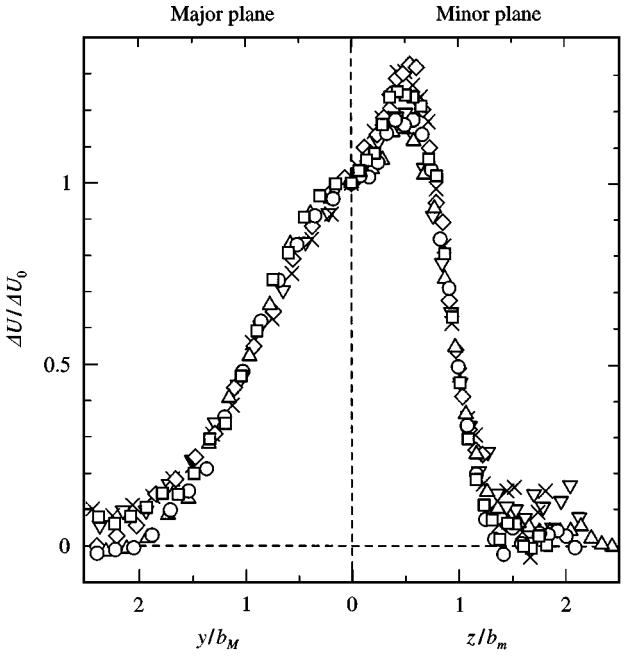

Figure 15. Distribution of velocity defect ΔU in major plane (on left) and in minor plane (on right): ▽, ($x/D = 12{\cdot}0$, AR $= 2{\cdot}0$); △, (12·0, 3·0); ×, (16·0, 2·0); o, (16·0, 3·0); ◇, (20·0, 2·0); □, (20·0, 3·0). ΔU_0 is value of ΔU on the x-axis.

produced on u' by the action of $-\overline{uv}(\mathrm{d}U/\mathrm{d}y)$ in the major plane and $-\overline{uw}(\mathrm{d}U/\mathrm{d}z)$ in the minor plane. u' is redistributed into v' and w' by the pressure–strain interaction.

The distribution of u' is approximately similar, as shown in Figure 17, if normalized by its value at the wake axis u'_0 and the half-widths b_M and b_m in the same manner as the velocity defect ΔU.

3.4.3. *Decay of velocity defect and turbulence intensity*

The maximum velocity defect $\Delta U_{\max}$ and the maximum turbulence intensity $u'_{\max}$ are plotted in Figure 18 against x. In the region $x/D > 14$, the decay of $\Delta U_{\max}$ and $u'_{\max}$ seem to be not inconsistent with the decay law of the axisymmetric far wake $x^{-2/3}$. This is also true for the equivalent half-width $b_e = (b_M b_m)^{1/2}$, which obeys the law $x^{1/3}$ in the same region (see Figure 19). The statistical properties in the far wake has been assumed to depend only on the integral properties of the body such as the drag and lift. Thus, the elliptic wake is expected to tend to the axisymmetric far wake. However, a large distance x appears to be needed, in view of the significant difference in the profiles of the time-mean and fluctuating velocities in the major and minor planes (Figures 13 and 16).

3.4.4. *Vortex formation region*

The x position where u' and w' attain a maximum at the centre of the wake can be interpreted as the end of formation region for the hairpin-like vortices in the minor plane. This is because the hairpin-like vortices acquire the maximum circulation there, then being

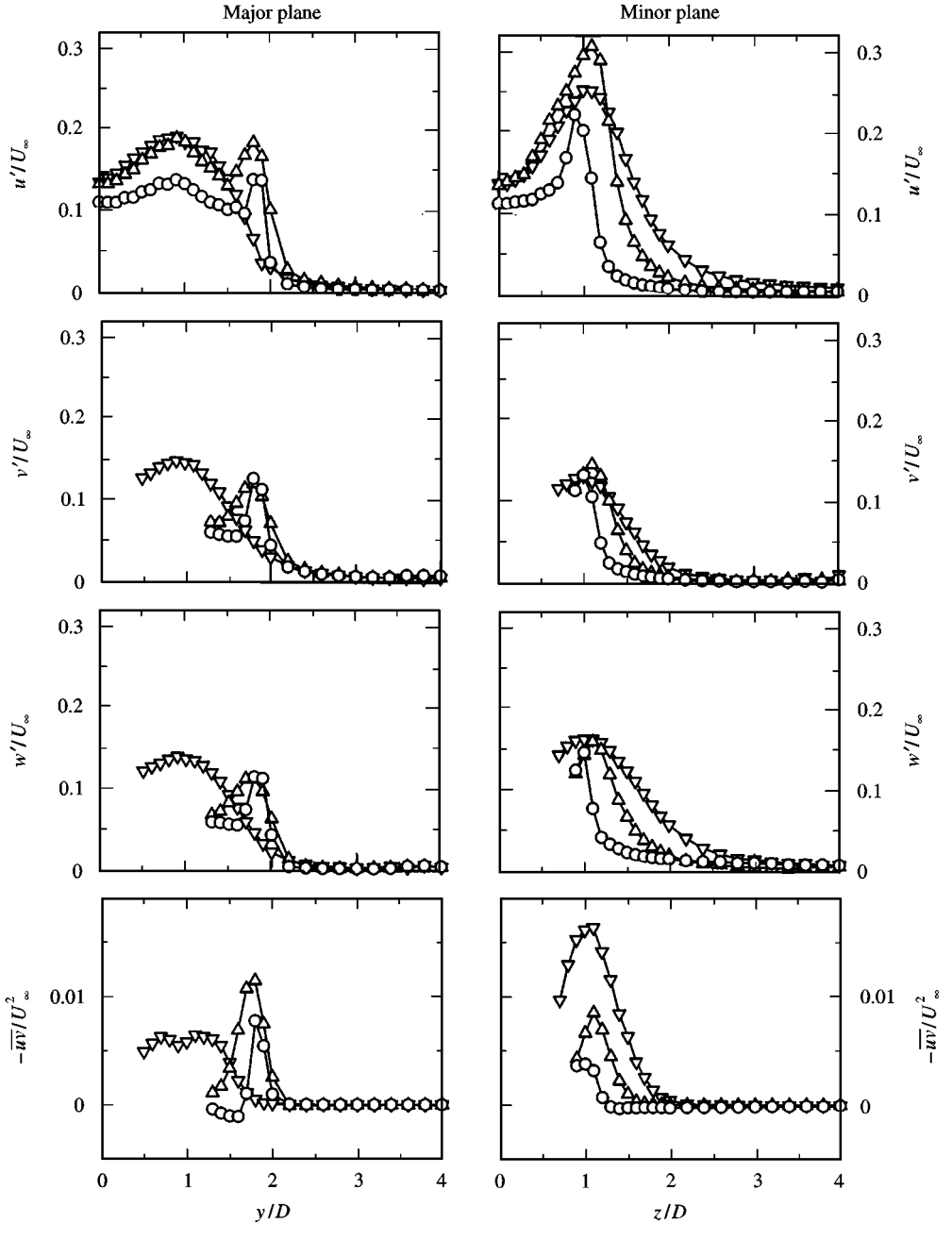

Figure 16. Distributions of turbulence intensities u', v', w' and Reynolds shear stresses $-\overline{uv}$, $-\overline{uw}$ for AR = 3·0: o, x/D = 1·0: △, 2·0; ▽, 4·0. u' was measured by split-film probe while v', w' and Reynolds stresses were measured by X-wire probe, being shown in regions where I_r is less than 0·2. Solid lines for visual aid only.

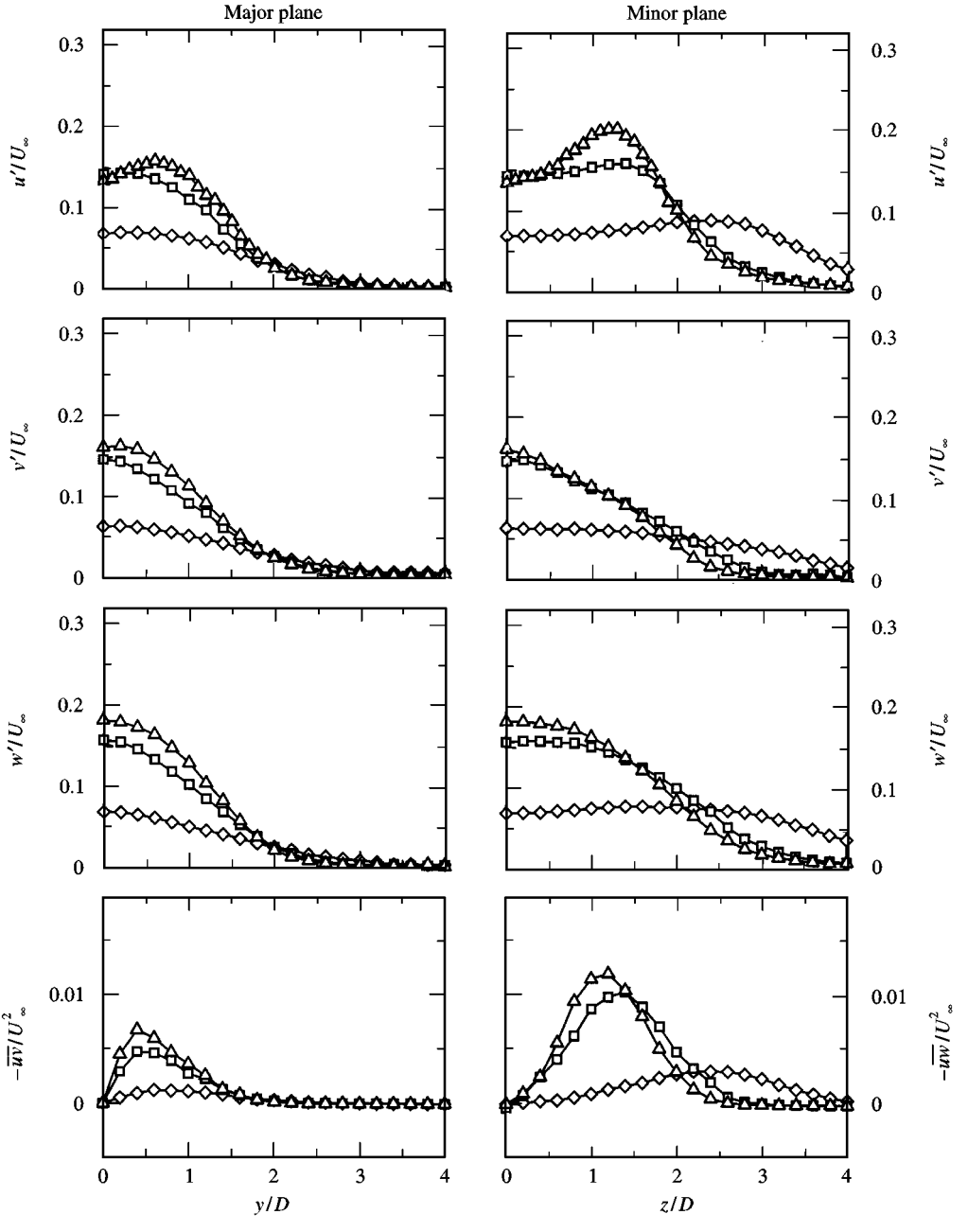

Figure 16. (Continued) Distributions of turbulence intensities u', v', w' and Reynolds shear stresses $-\overline{uv}$, $-\overline{uw}$ for AR = 3·0. △, x/D = 6·0: □, 8·0; ◇, x/D = 20·0. u' was measured by I-wire probe while v', w' and Reynolds stresses were measured by X-wire probe. Solid lines for visual aid only.

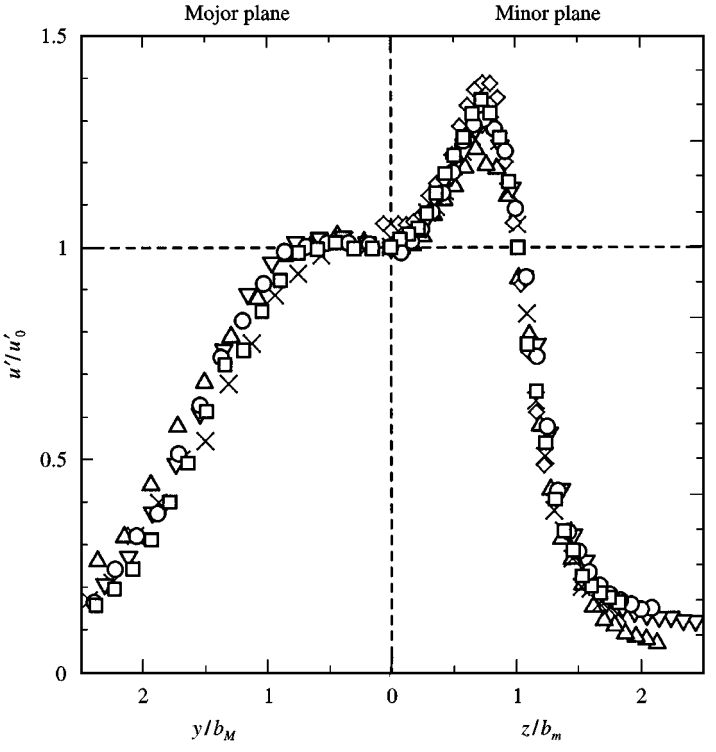

Figure 17. Distribution of turbulence intensity u' in major plane (on left) and in minor plane (on right): ▽, ($x/D = 12{\cdot}0$, AR $= 2{\cdot}0$); △, (12·0, 3·0); ×, (16·0, 2·0); o, (16·0, 3·0); ◇, (20·0, 2·0); □, (20·0, 3·0). u'_0 is the value of u' on the x-axis.

shed downstream with a slow decay of the circulation. The maximum circulation is expected to generate the highest intensity of u' and w' on the centre of the wake. The turbulence intensities u' and w' plotted against x (not shown) revealed that they attain a broad maximum at a position between $x/D = 5$ and 6; this can also be seen in Figure 15. Thus, the end of the formation region lies in this region. This is also supported by the fact that the peak value of an averaged power spectrum at the frequency F_m (say E_m) attains a maximum at $x/D = 6{\cdot}0$ (Figure 20). The averaged spectrum was obtained by averaging the power spectra measured at different z positions at a fixed x, thus the peak value being a measure of amplitude of u^2 averaged along the z-direction.

It may be noted that the formation region for vortices in the major plane cannot be identified on the basis of the turbulence intensities on the wake axis. This is because these vortices are weaker than the hairpin-like vortices, as indicated by higher u' in the minor plane than that in the major plane (Figure 16), so that the level of the turbulence intensities on the wake axis is determined by the hairpin-like vortices. However, the peak value of the averaged spectrum at F_M (say E_M) yields information on the formation region (Figure 20). The peak value E_M attains a peak at $x/D = 4{\cdot}0$, suggesting that this is the end of the formation region for the vortices in the major plane.

3.5. Low-Frequency Unsteadiness of Vortex Shedding

Velocity fluctuations associated with the periodic vortex shedding have low-frequency amplitude modulation. This has been found in the vortex-street wake of a circular cylinder

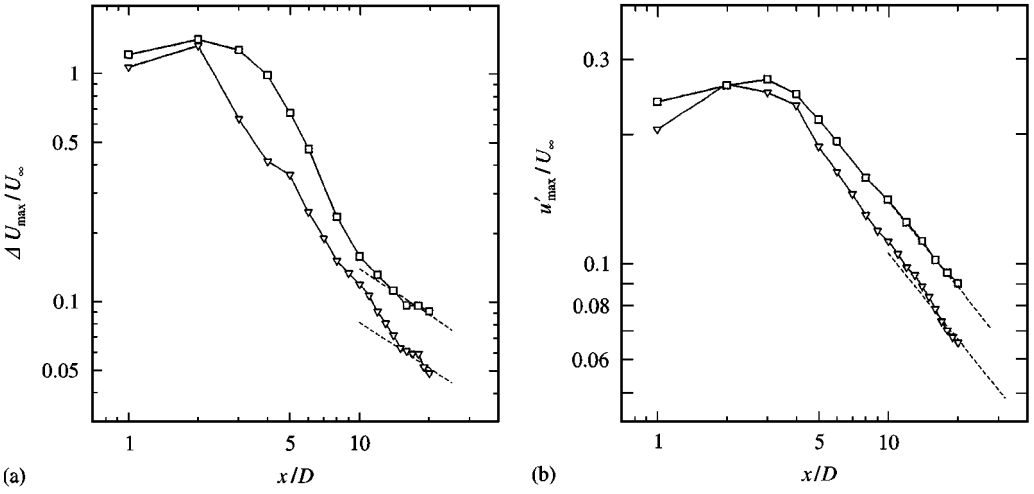

Figure 18. Decay of (a) maximum velocity defect ΔU_{max} and (b) maximum turbulence intensity u'_{max}. ▽, AR = 2·0; □, AR = 3·0. - - -, $x^{-2/3}$. Solid lines for visual aid only.

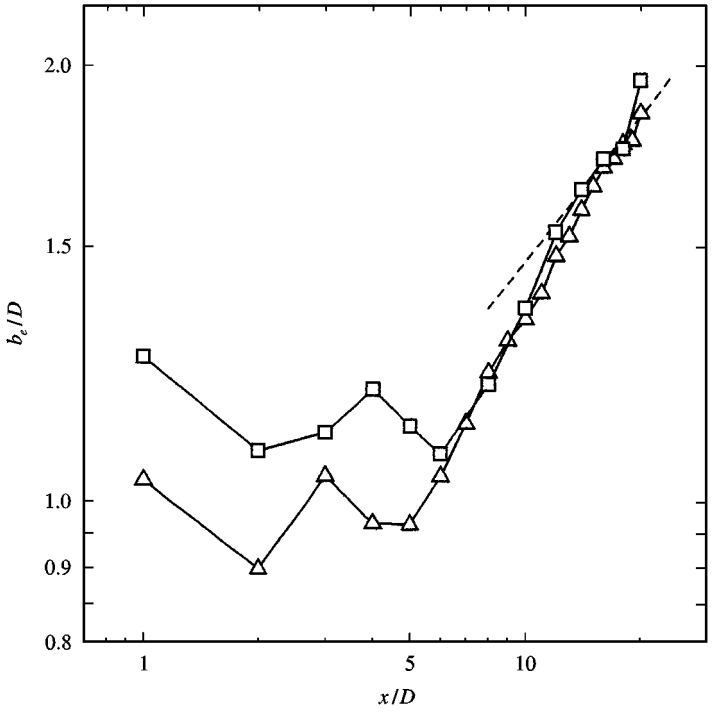

Figure 19. Half-width as function of longitudinal distance: △, AR = 2·0; □, AR = 3·0. - - -, $x^{1/3}$. Solid lines for visual aid only.

(Williamson 1992; Kiya & Ishikawa 1997;) and a plate normal to the flow (Najjar & Balachandar 1998), and in a plane mixing layer (Ishikawa *et al.* 1997). Statistical properties of the amplitude modulation can be studied by the wavelet transform of the velocity fluctuation u. The Morlet wavelet was used to obtain the real part W_R and the

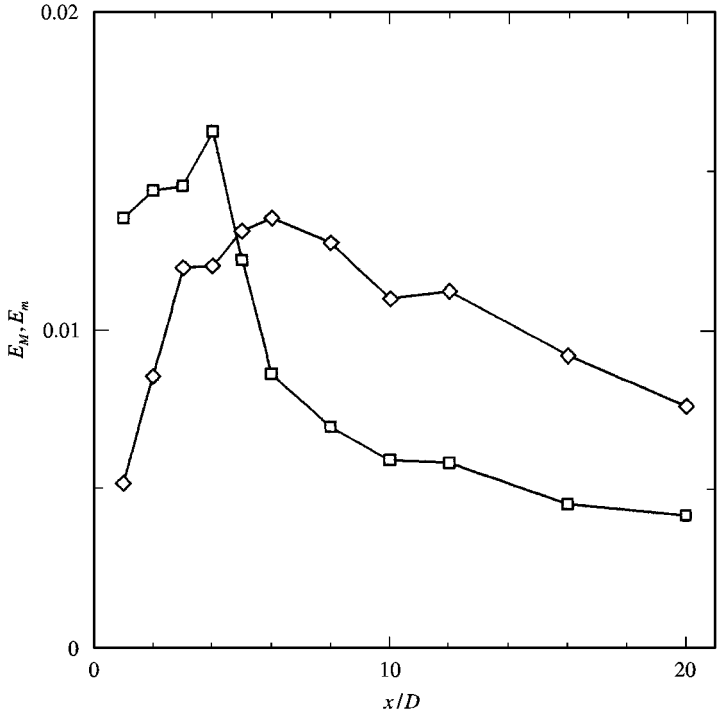

Figure 20. Peak value of averaged power spectrum at F_M and F_m as function of longitudinal distance for AR = 3·0. □, E_M (major plane); ◇, E_m (minor plane). Solid lines for visual aid only.

imaginary part W_I of the wavelet coefficient $W(a, b)$ defined by

$$W(a, b) = \frac{1}{\sqrt{a}} \int \psi^* \left(\frac{t-b}{a} \right) u(t)\, \mathrm{d}t, \tag{2}$$

where $\psi(T) = \exp(\mathrm{i}k_\psi T)\exp(-T^2/2)$ is the Morlet wavelet, and the asterisk denotes the complex conjugate; a is the scale parameter and b is the translation. The parameter k_ψ was chosen as 6·0 as recommended by Farge (1992).

Amplitude of the real part follows the amplitude of the velocity fluctuation if the scale a is fixed at the inverse of the vortex-shedding frequency, that is, a high amplitude of u corresponds to a high amplitude of W_R, and *vice versa*. On the other hand, a high amplitude of the imaginary part W_I corresponds to a high amplitude of $\partial u/\partial t$ because the imaginary part of $\psi(t)$ is antisymmetric. Thus, the time history of modulus $|W|$ $(= (W_R^2 + W_I^2)^{1/2})$ is the envelope of the time history of the real part and the imaginary part. This implies that the fluctuating part of the modulus includes information on the amplitude modulation of the velocity fluctuation. This amplitude modulation will be referred to as the low-frequency unsteadiness of the shed vortices.

The low-frequency unsteadiness was studied for both disks AR = 2·0 and 3·0. In what follows, the results for AR = 3·0 will be presented because features of the unsteadiness were basically the same in both cases.

Figure 21(a) shows contours of those W_R and $|W|$ in the (a,b) parameter space, which were constructed from u near the edge of the wake in the minor plane. High peaks of W_R appears at the scale $a/\Delta t = 1/(F_m \Delta t) = 24{\cdot}0$, which is the period of the vortex shedding. Here, $\Delta t = 0{\cdot}5$ ms is the time interval of digitization of u. At the same scale, $|W|$ attains peaks with

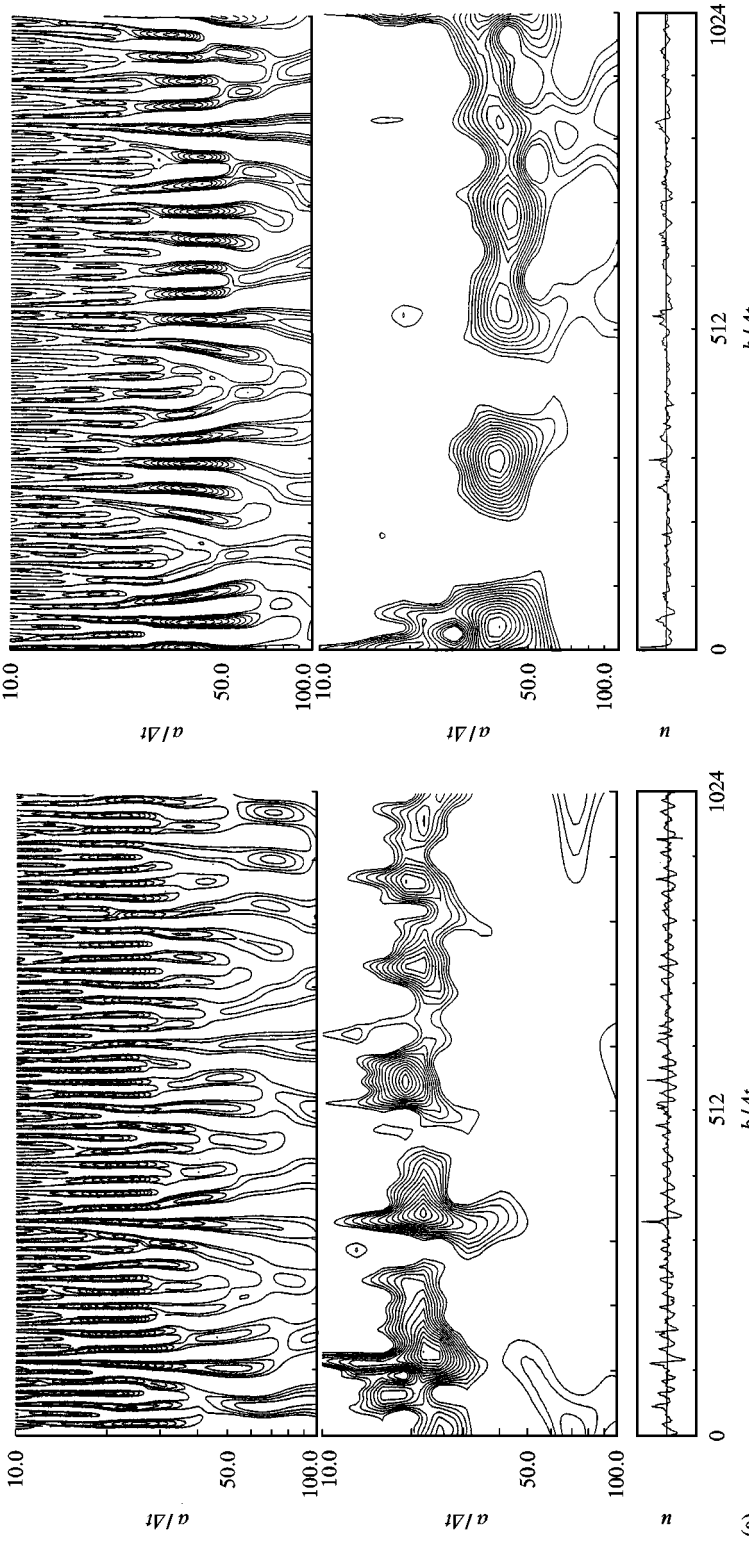

Figure 21. Morlet wavelet transform of u at (a) $(x/D, y/D, z/D) = (4{\cdot}0, 0{\cdot}0, 2{\cdot}0)$ in minor plane and (b) $(x/D, y/D, z/D) = (4{\cdot}0, 2{\cdot}0, 0{\cdot}0)$ in major plane for AR = 3·0. $\Delta t = 0{\cdot}5$ ms is interval of digitization of u. Top, real part W_R (positive values only); middle, modulus $|W|$ (values greater than 30% of maximum $|W|$); bottom, u.

an interval much longer than that for W_R. This is interpreted as low-frequency unsteadiness. Similar results are obtained for the velocity fluctuations in the major plane as shown in Figure 21(b). In this case, the high peaks of W_R appear at the scale $a/\Delta t = 1/(F_M \Delta t) = 41{\cdot}0$.

Figure 22 shows the simultaneous fluctuating components of modulus in the major and minor planes, $|W|'_M$ and $|W|'_m$, respectively. The velocity fluctuations were measured at the same positions as in Figure 21. The representative frequency of the low-frequency unsteadiness can be obtained in terms of the power spectrum of the fluctuating component, which is shown in Figure 23. The spectrum in the minor plane has a broad peak at a frequency in a range 15–20 Hz, while that in the major plane has a broad peak at a frequency in another

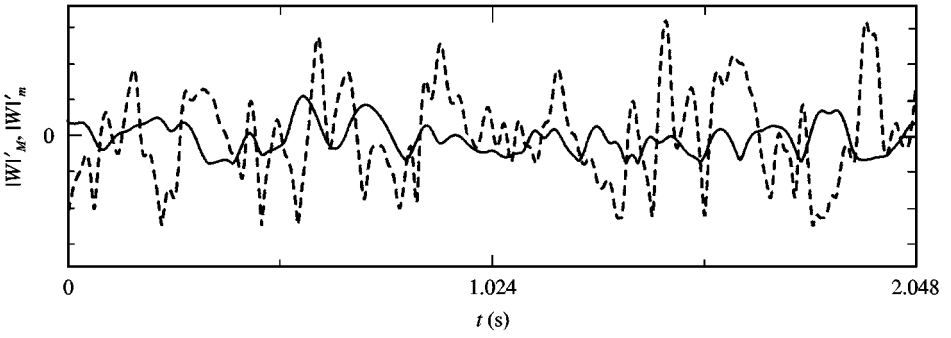

Figure 22. Time history of fluctuating part of modulus in major plane at scale $a/\Delta t = 24{\cdot}0$, $|W|'_M$, and that in minor plane at $a/\Delta t = 41{\cdot}0$, $|W|'_m$, for AR = 3·0. Vertical scale is arbitrary linear. Positions of measurement are the same as those in Figure 21. ——, $|W|'_M$; - - -, $|W|'_m$.

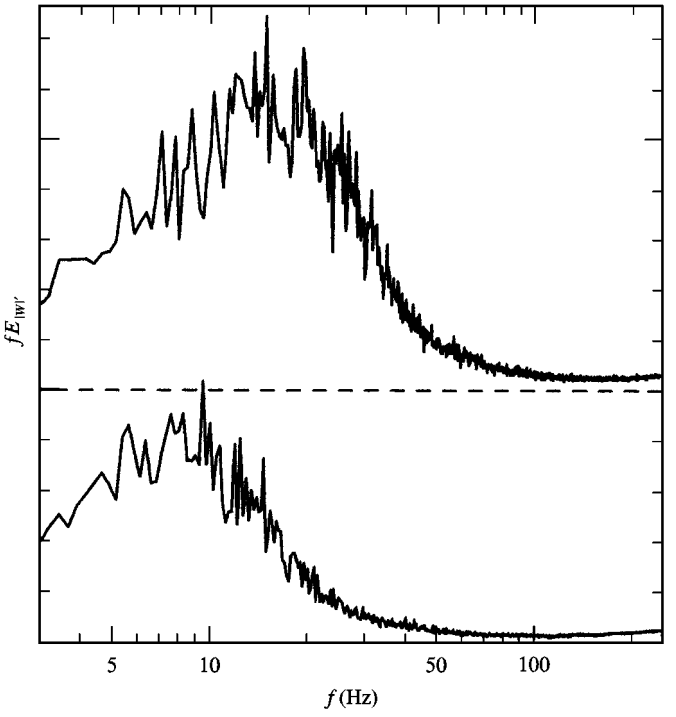

Figure 23. Power spectrum of $|W|$' in minor plane ($a/\Delta t = 24{\cdot}0$) and major plane ($a/\Delta t = 41{\cdot}0$) for AR = 3·0. The vertical axis is arbitrary linear. Top, minor plane; bottom, major plane.

range 7–10 Hz. These representative frequencies are of the order of 1/5 of the corresponding vortex-shedding frequencies F_m and F_M. In other words, every five shed vortices experience modulation in their strength. This was also the case for the elliptic disk of AR = 2·0. In passing, it is worth mentioning that the representative frequency for the vortex-street wake of a circular cylinder is of the order of 1/25 of the vortex-shedding frequency at Reynolds numbers of 80–10^4 (Kiya & Ishikawa 1997).

Another aspect of the low-frequency unsteadiness can be obtained in terms of the cross-correlation of $|W|'$ constructed from simultaneous velocity fluctuations at two opposite positions in each plane, a sample record of the $|W|'$ being given in Figure 24. Figure 25 shows the cross-correlation of $|W|'_+$ and $|W|'_-$ in the minor plane, $C_m(\tau)$, where τ is the time lag; $|W|'_+$ is $|W|'$ on the side $z > 0$ while $|W|'_-$ is that on the opposite side, $z < 0$. The velocity fluctuations used to construct $|W|'_+$ and $|W|'_-$ are those at positions of maximum u'. The cross-correlation takes a significant positive value of approximately 0·35 at $\tau = 0$. This is also the case for the cross-correlation $C_M(\tau)$ in the major plane. The above results indicate that the low-frequency unsteadiness in the minor plane, for example, occurs in phase on both sides. The same is true in the major plane. If the high amplitudes of the velocity fluctuation are assumed to correspond to stronger shed vortices and thus a greater instantaneous width of the wake, the greater width should appear simultaneously on both sides in each plane. The reverse is true for the low amplitudes of the velocity fluctuation.

The phase relation of the low-frequency unsteadiness in the major and minor planes can be obtained in terms of the cross-correlation coefficient of the fluctuating components of modulus $|W|'_M$ and $|W|'_m$ [say, $C_{Mm}(\tau)$] based on the simultaneous velocity fluctuations. The fluctuating components have been presented in Figure 22. As shown in Figure 26, $C_{Mm}(\tau)$ attains a significant negative value of $-0{\cdot}4$ for AR = 2·0 and $-0{\cdot}25$ for AR = 3·0 at $\tau = 0$, indicating that the unsteadiness in the two planes is out of phase. That is, when the wake is in the phase of enlargement in the major plane, the wake in the minor plane is in the phase of shrinkage, and *vice versa*. The same results were obtained in a range $x/D = 2{\cdot}0$–$8{\cdot}0$, so that the low-frequency modulation is of large spatial extent.

4. DISCUSSION

We conjecture that the mechanism responsible for the two periodic components is the global instability in the steady, recirculating near wake as in the case of the periodic vortex

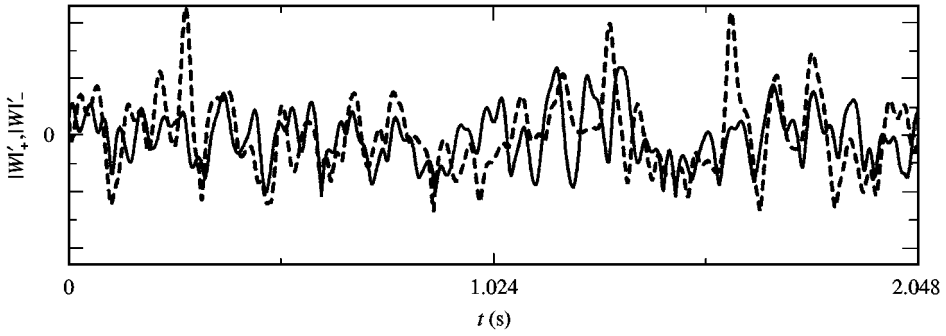

Figure 24. Time history of fluctuating component of modulus at positions of maximum u' in minor plane for AR = 3·0: $|W|'_+$ on side $z > 0$ and $|W|'_-$ on side $z < 0$ ($a/\Delta t = 24{\cdot}0$). ——, $|W|'_+$; - - -, $|W|'_-$. Vertical axis is arbitrary linear.

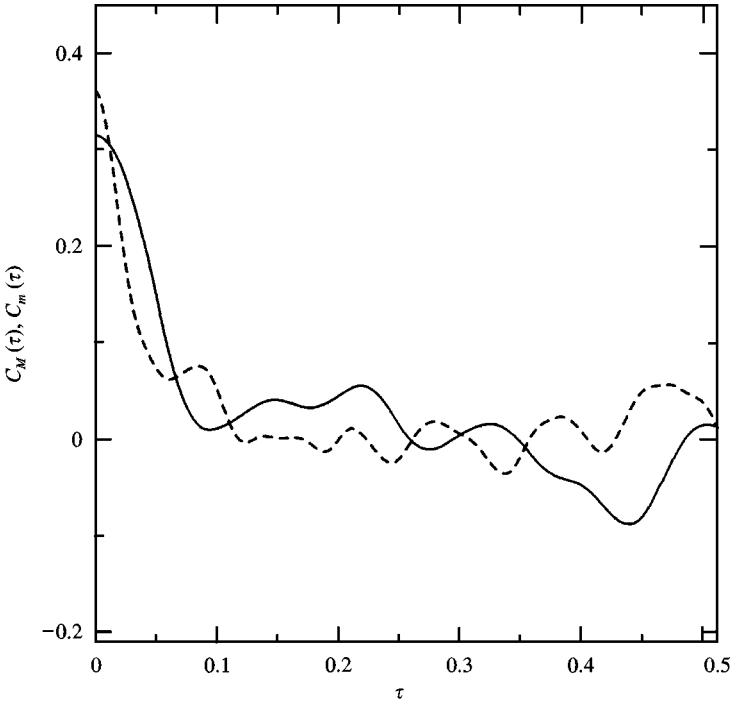

Figure 25. Cross-correlation coefficient of modulus $|W|'_+$ and $|W|'_-$ in major plane ($a/\Delta t = 24{\cdot}0$) and in major plane ($a/\Delta t = 41{\cdot}0$) for AR = 3·0. ——, C_M (major plane); - - -, C_m (minor plane).

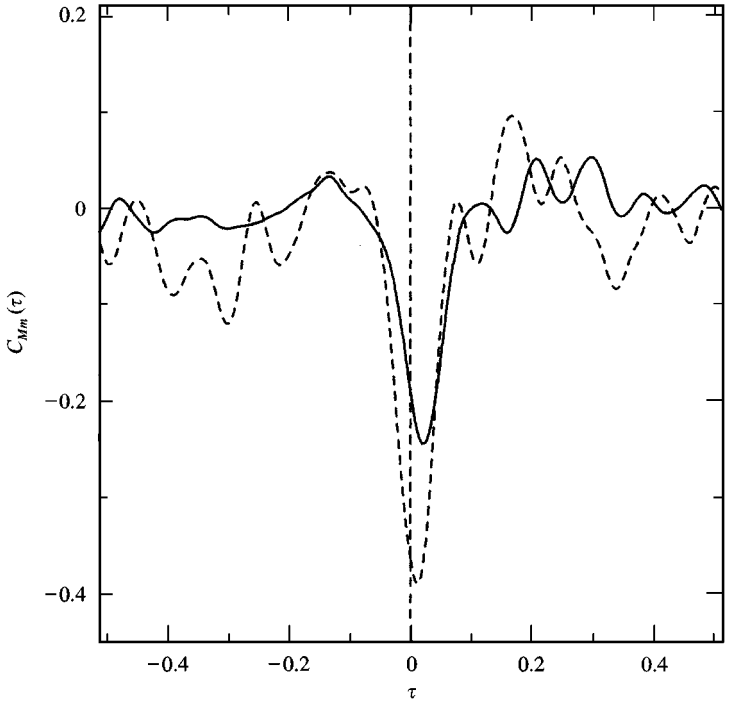

Figure 26. Cross-correlation coefficient of $|W|'_M$ and $|W|'_m$ at positions of maximum u', C_{Mm}(t), at $x/D = 4{\cdot}0$. ——, AR = 2·0; - - -, AR = 3·0.

shedding in the near wake of two-dimensional bluff bodies (Huerre and Monkewitz 1990; Asai *et al.* 1996). If the Reynolds number is sufficiently low, a steady recirculating region is realized in the near wake of the disk. The velocity profile in the recirculating region has two representative length scales; one is the width of the wake in the minor plane, and the other is that in the major plane. The velocity profile in the minor plane is expected to have the fundamental mode of maximum growth rate at a critical Reynolds number. This eventually evolves into the alternate shedding of the hair-pin vortices (Figure 4). The same should also be true in the major plane although the flow visualization has not demonstrated vortical structures associated with this mode.

The point is that the fundamental modes in the minor and major planes have different frequencies and growth rates. This is the reason why two periodic velocity components appear in the elliptic wake. The growth rate is likely to be greater in the minor plane than in the major plane. This is because the level of the velocity fluctuation u' in the region $x/D < 6$ is higher in the minor plane than in the major plane (Figure 16) and also because the region of the component F_M is eroded by that of the component F_m with increasing longitudinal distance in the same region (Figure 8).

If the above interpretation is correct, two periodic components are expected to appear also in the wake of a rectangular plate. This is the case as shown in Figures 7 and 9. The Strouhal number for the elliptic disks is only slightly different from that for the rectangular plates at the same value of AR. This suggests that the velocity distribution in the steady recirculating region and thus the vortical structure caused by the instability are similar in the two wakes.

The vortical structure responsible for the periodic component in the major plane has not been observed in the flow visualization. To study this structure, a direct numerical simulation of the wake of a rectangular plate was made by NAGARE3D.DH software produced by the Institute of Computational Fluid Dynamics Co. Ltd, Tokyo. This software employs the third-order upwind-difference scheme of Kawamura & Kuwahara (1984) for the nonlinear inertial terms. The rectangular plate has the thickness of $D/3$, D being the length of the shorter side, and the aspect ratio AR $= 2{\cdot}0$. Reynolds number based on D is 200. The flow was impulsively started from rest with the velocity U_∞. The plate was forced to oscillate in the y- and z-directions with the frequency F_M and F_m (Figure 7), respectively, and the same amplitude of $0{\cdot}05D$ to enhance the vortex shedding. The forcing was stopped at $U_\infty t/D = 69{\cdot}1$, and then the computation was continued up to $U_\infty t/D = 203{\cdot}8$. This time interval of 134·7 corresponds approximately to 16 periods of shedding of the hairpin-like vortices in the minor plane, or 11 periods of shedding of a structure responsible for F_m. Thus, the effects of the forcing on the flow is expected to have disappeared at time $U_\infty t/D = 203{\cdot}8$.

Figure 27 shows isosurfaces of magnitude of vorticity vector in the wake at the time $U_\infty t/\mathrm{D} = 180{\cdot}0$. Hairpin-like vortices are alternately shed on both sides of the wake in the minor plane, while in the major plane these hairpin-like vortices appear to experience a meandering motion. Thus, the structure responsible for the component F_M is this meandering motion. The meandering motion might be associated with large-scale vortices in the major plane although they are not clear in the simulation; these vortices might become clearer at higher Reynolds numbers. The hairpin-like vortices emerge from the end of the recirculating region, not being a result of deformation of rectangular vortex rings which one might imagine are shed from the edge of the plate. Moreover, the power spectrum of velocity fluctuation u in the wake, which was obtained in terms of u during the time interval 167·0–203·8, was found to have a peak at the frequency almost equal to F_M and F_m in the major and minor planes (not shown). These facts strongly suggest that the frequencies F_M and F_m are associated with the fundamental frequency of global instability in the near

wake. A theoretical or numerical analysis of the global instability of the wake is a challenging problem to be tackled in the future.

A comparison between Figures 4 and 27 reveals that the hairpin-like vortices emerge more downstream in the simulation than in the flow visualization. This is probably because the grid size for the simulation was not fine enough to capture details of the separated shear layer near the plate. Essential physics of the global instability in the flow, however, is likely to be captured by this simulation. More detailed simulations are needed in the future.

Figure 27 seems to suggest that the axis-switching is a result of different growth rates of the fundamental mode of the global instability in the major and minor planes. The fundamental mode in the minor plane, which generates the hairpin-like vortices, has a greater growth rate than that in the major plane, thus quickly increasing the width of the near wake in the minor plane. This is likely to be supported by the fact that the heads of the hairpin-like vortices travel up to $z/D = -2{\cdot}4$ or $2{\cdot}2$ in the region $x/D = 8$–10 [Figure 27(b)], while the meandering motion in the major plane moves the hairpin-like vortices towards the y-direction only to $z/D = -1{\cdot}1$ or $1{\cdot}5$ in the same region [Figure 27(a)]. This causes the axis-switching.

The average distance between shed vortices is approximately $6{\cdot}0D$ in the minor plane, so that the representative wavelength of the low-frequency unsteadiness is of the order of $30{\cdot}0D$ because five consecutive vortices, on average, are included in one period of the unsteadiness. Thus, the low-frequency unsteadiness is of large spatial extent.

Low-frequency unsteadiness of the same nature has been observed in separated-and-reattaching flows (Eaton & Johnston 1982; Kiya 1989) and in the vortex-street wake of cylindrical bodies (Williamson 1992; Ishikawa *et al.* 1997). The unsteadiness in the separation bubbles is explained by a feedback loop. On the other hand, the unsteadiness in the vortex-street wake is interpreted as the large-scale vortex dislocations (Williamson 1992) or as the beat of two slightly different frequencies of the vortex shedding at nearby spanwise positions. In the elliptic wake, it is difficult to assume vortex dislocations or a feedback loop. Moreover, since $F_m = 85$ Hz and $F_M = 50$ Hz for AR $= 3{\cdot}0$, the beat frequency should be 35 Hz, which is more than twice the representative frequency of the unsteadiness in the minor plane and five times that in the major plane. Thus, the beat frequency is not consistent with the observed frequency of the unsteadiness. The mechanism of the low-frequency unsteadiness in the elliptic wake remains to be clarified.

5. CONCLUDING REMARKS

The present paper has described properties of turbulent wake of the elliptic disks of aspect ratio of $2{\cdot}0$ and $3{\cdot}0$. The main results may be summarized as follows.

(a) There are two periodic components of velocity fluctuations in the elliptic wake. One is in the minor plane, while the other is in the major plane. The component in the minor plane is associated with the alternate shedding of hairpin-like vortices. A structure responsible for the component in the major plane has not been visualized but is likely to be a meandering motion of the wake in the same plane. The meandering motion is confirmed by a numerical simulation at a Reynolds number of 200. Both components were discussed, and it was suggested that they are associated with the global instability of the steady recirculating region behind the elliptic disk.

(b) The frequencies of the periodic velocity fluctuations, normalized in the form of Strouhal numbers, are functions of the aspect ratio. No universal Strouhal number is constructed by merely adjusting the length scale.

(c) The axis switching, which is manifested as the cross-over of the half-width in the major plane and that in minor plane, occurs approximately 4 minor diameters behind the disk. The mechanism of the axis switching is different from that in elliptic jets. In the elliptic wake, the axis switching is discussed to be due to the difference in the growth rates of the fundamental modes in the major and minor planes. This is likely to be confirmed by the numerical simulation. A theoretical or numerical analysis of the global instability is a challenging problem to be tackled in the future.

(d) The maximum velocity defect, the maximum longitudinal turbulence intensity and the equivalent half-width of the elliptic wake obey the law for the far wake of axisymmetric bodies, farther downstream than approximately 15 minor diameters behind the disk. However, a much longer distance appears to be needed before the wake acquires the same statistical properties as an axisymmetric wake.

(e) The wake experiences a low-frequency unsteadiness. This was suggested from the wavelet analysis of the longitudinal velocity fluctuations in the minor and major planes, using the fluctuating component of modulus of the Morlet wavelet transform. The representative frequency of the unsteadiness is different in the two planes, being approximately one-fifth of the frequency of the vortex shedding in the minor plane and that of the meandering motion in the major plane. The unsteadiness is in phase on both sides of the wake in the same plane but out of phase in the different planes. The unsteadiness is of large spatial extent, being, for example, 30 minor diameters in the minor plane for AR = 3·0. This could be compared with the distance between two consecutive vortices in the minor plane, which is approximately 6 minor diameters. The mechanism responsible for the unsteadiness remains to be clarified.

ACKNOWLEDGEMENTS

The authors express their sincere thanks to Dr O. Mochizuki for his advice on the hot-wire and split-film measurements, to Mr T. Sampo for his help in the construction of the experimental apparatus, and to Mr N. Yamamoto for his help in the numerical simulation.

References

Achenbach, E. 1974 Vortex shedding from spheres. *Journal of Fluid Mechanics* **62,** 209–221.

Asai, M., Nakagawa, H. & Nishioka, M. 1996 Wake instability and frequency selection of the von Karman vortex shedding. *Journal of Japan Society for Aeronautical and Space Sciences* **44,** 251–256 (in Japanese).

Berger, E., Scholz, D. & Schumm, M. 1990 Coherent vortex structures in the wake of a sphere and a circular disk at rest and under forced vibrations. *Journal of Fluids and Structures* **4,** 231–257.

Cannon, S., Champagne, F. & Glezer, A. 1993 Observations of large-scale structures in wakes behind axisymmetric bodies. *Experiments in Fluids* **14,** 447–450.

Chandrsuda, C. & Bradshaw, P. 1981 Turbulence structure of a reattaching mixing layer. *Journal of Fluid Mechanics* **110,** 171–194.

Chevray, R. 1968 The turbulent wake of a body of revolution. *ASME Journal of Basic Engineering* **90,** 275–284.

Eaton, J. K. & Johnston, J. P. 1992 Low-frequency unsteadiness of a reattaching turbulent shear flow, In *Turbulent Shear Flows*, Vol. 3 (eds L.J.S.Bradbury *et al.*), pp. 162–170. Berlin: Springer-Verlag.

Farge, M. 1992 Wavelet transform and their applications to turbulence. *Annual Review of Fluid Mechanics* **24,** 395–457.

Fuchs, H. V., Mercker, E. & Michel, U. 1979 Large-scale coherent structures in the wake of axisymmetric bodies. *Journal of Fluid Mechanics* **93,** 185–207.

Ho, C.M. & Gutmark, E. 1987 Vortex induction and mass entrainment in a small-aspect-ratio elliptic jet. *Journal of Fluid Mechanics* **179,** 383–405.

HUERRE, P. & MONKEWITZ, P. A., 1990, Local and global instabilities in spatially developing flow. *Annual Review of Fluid Mechanics* **22,** 473–537.

HUSSAIN, F. & HUSAIN, H. S. 1989 Elliptic jets. Part 1. Characteristics ofunexcited and excited jets. *Journal of Fluid Mechanics* **208,** 257–320.

HWANG, N. H. C. & BALDWIN, L. V. 1966 Decay of turbulence in axisymmetric wakes. *ASME Journal of Basic Engineering* **88,** 261–267.

ISHIKAWA, H., KIYA, M. & MOCHIZUKI, O. 1997 POD and wavelet analyses of coherent structures in a turbulent mixing layer. *Proceedings of International Conference on Fluid Engineering, The JSME Centennial Grand Congress*, Vol. 2, pp. 583–588. Tokyo: The Japan Society of Mechanical Engineers.

KAWAMURA, T. & KUWAHARA, L. 1984 Computation of high Reynolds-number flow around a circular cylinder with surface roughness. AIAA Paper 84–0340.

KIM, H.J. & DURBIN, P.A. 1988 Observations of the frequencies in a sphere wake and of drag increase by acoustic excitation. *Physics of Fluids* **31,** 3260–3265.

KIYA, M. 1989 Separation bubbles. In *Theoretical and Applied Mechanics* (eds P. Germain *et al.*), pp. 173–191. Amsterdam: North-Holland.

KIYA, M. & ISHIKAWA, J. 1998 Coherent structures and large low-frequency irregularity in free turbulent shear flows educed by wavelet transform and proper orthogonal decomposition. *Proceedings of the 2nd China-Japan Workshop on Turbulent Flows* (ed. Q.D. Wei), pp. 8–22. Beijing: Beijing University.

MONKEWITZ, P. A. 1988 A note on vortex shedding from axisymmetric bluff bodies. *Journal of Fluid Mechanics* **192,** 561–575.

NAJJAR, F. M. & BALACHANDAR, S. 1998 Low-frequency unsteadiness in the wake of a normal plate. *Journal of Fluid Mechanics* **370,** 101–147.

PETERSON, C. W., STRICKLAND, J. H. & HIGUCHI, H. 1996 The fluid dynamics of parachute inflation. *Annual Review of Fluid Mechanics* **28,**361–387.

SAKAMOTO, H. & HANIU, H. 1990 A study of vortex shedding from spheres in a uniform flow. *ASME Journal of Fluids Engineering* **112,** 386–392.

SHIRAYAMA, S. 1992 Flow past a sphere: Topological transitions of the vorticity field. *AIAA Journal* **30**, 349–358.

TANEDA, S. 1978 Visual observation of the flow past a sphere at Reynolds numbers between 10^4 and 10^6. *Journal of Fluid Mechanics* **85,** 187–192.

UBEROI, M. S. & FREYMUTH, P. 1970 Turbulent energy balance and spectra of the axisymmetric wake. *Physics of Fluids* **13,** 2205–2210.

WILLIAMSON, C. H. K. 1992 The natural and formation of spot-like 'vortex dislocations' in the transition of a wake. *Journal of Fluid Mechanics* **243,** 393–441.

WU, J.-S. & FAETH, G. M. 1993 Sphere wakes in still surroundings at intermediate Reynolds numbers. *AIAA Journal* **31**, 1448–1455.

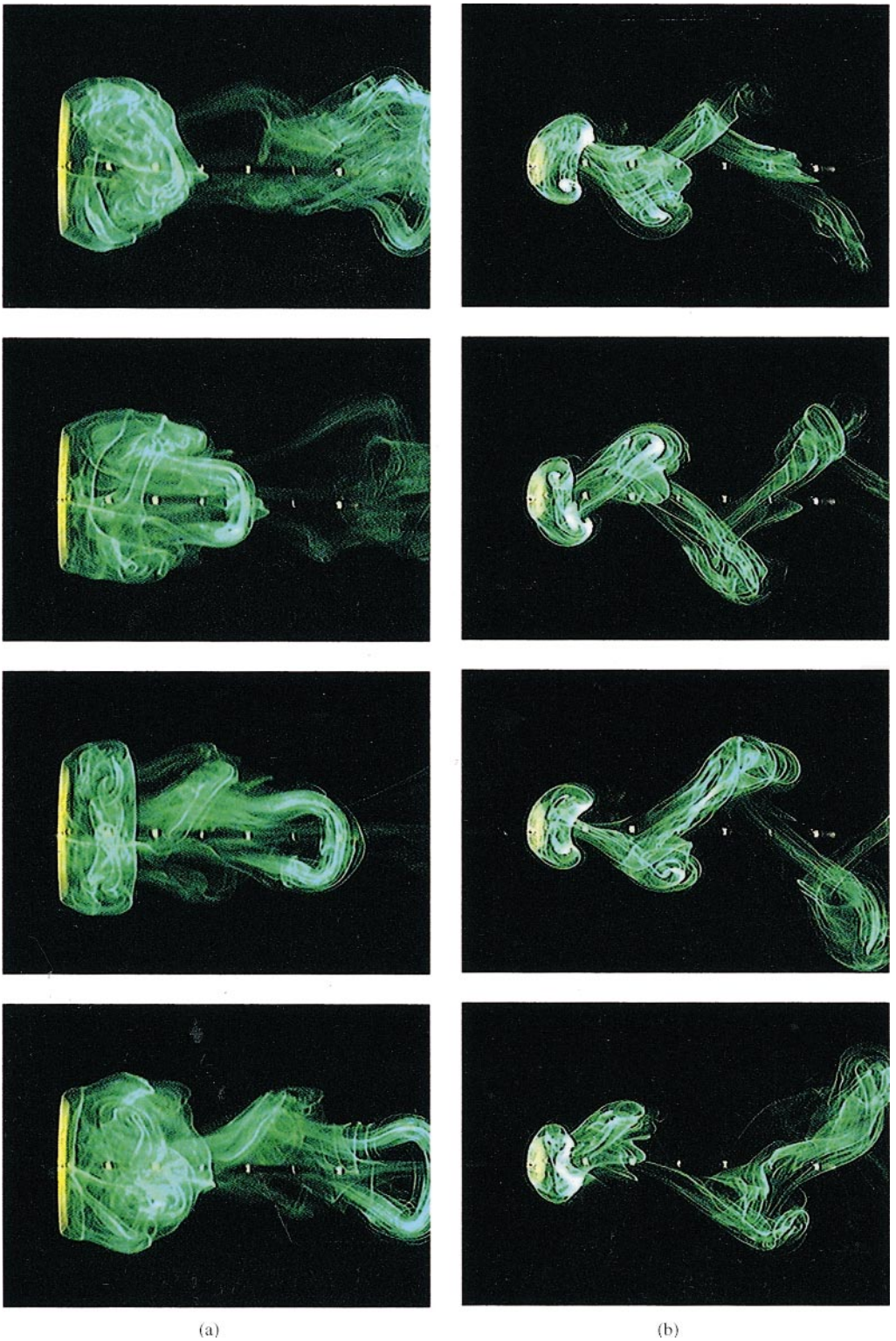

Figure 4. Flow visualization by fluorescent dye at Re = 200 in (a) major plane and (b) minor plane for AR = 3·0. Flow from left to right. Time advances from top to bottom with interval of $3{\cdot}0D/U_\infty$, which is approximately one-third of vortex-shedding period. Flow patterns in (a) and (b) are not simultaneous.

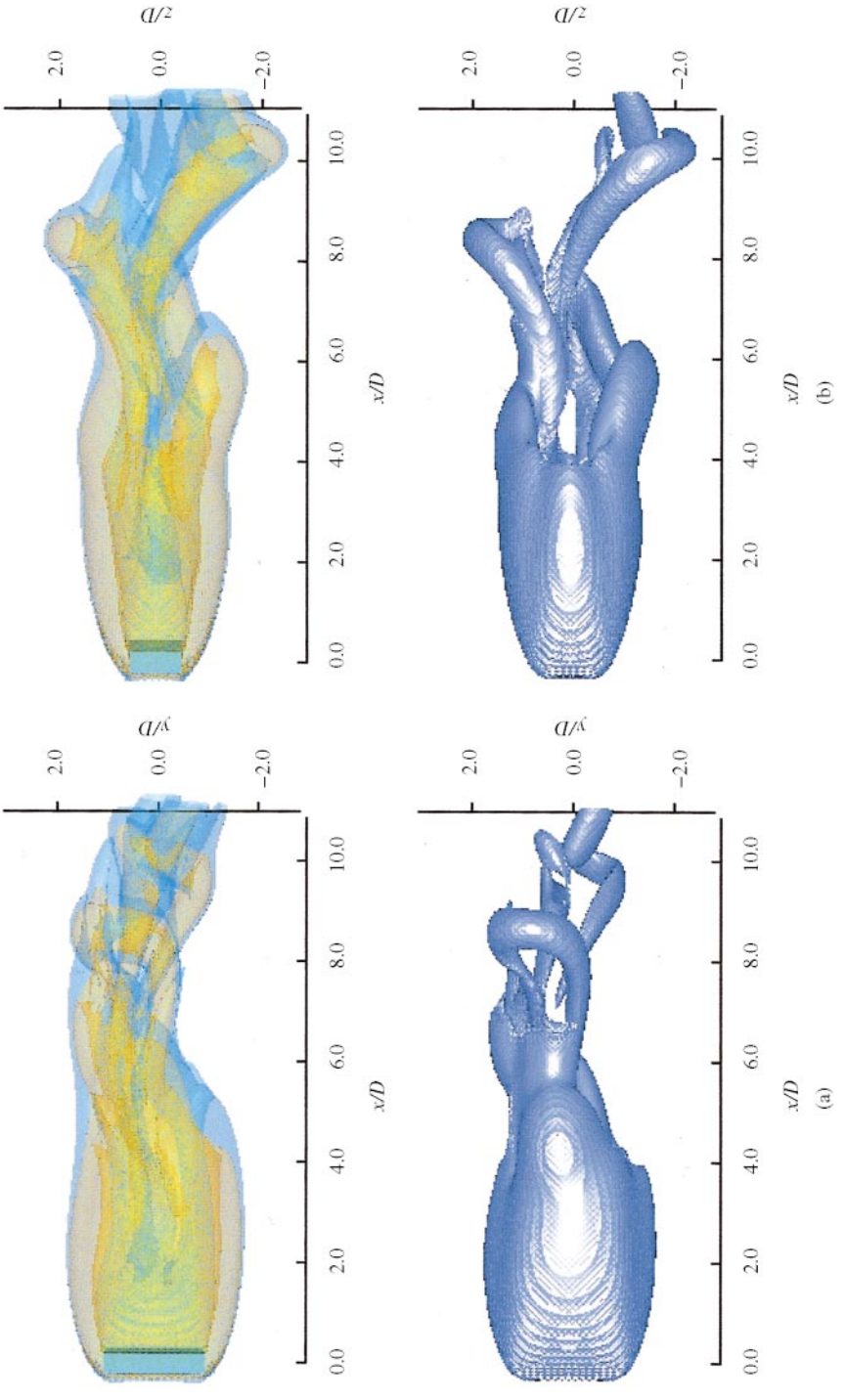

Figure 27. Vorticity contours in simulated wake of rectangular plate of thickness $D/3$ and aspect ratio $\mathrm{AR} = 2{\cdot}0$ at $\mathrm{Re} = 200$ in (a) major plane and (b) minor plane. Top and bottom figures in (a) and (b) are different visualizations of vorticity of the same flow.